Cellular and Molecular Life Sciences (2022) 79:164
https://doi.org/10.1007/s00018-022-04172-x

ORIGINAL ARTICLE

MCL1 alternative polyadenylation is essential for cell survival and mitochondria morphology

Isabel Pereira-Castro[1,2] · Beatriz C. Garcia[1,2] · Ana Curinha[2,7] · Ana Neves-Costa[3] · Eduardo Conde-Sousa[4,5] · Luís F. Moita[3] · Alexandra Moreira[1,2,6]

Received: 17 August 2021 / Revised: 7 January 2022 / Accepted: 27 January 2022 / Published online: 1 March 2022

Abstract

Alternative polyadenylation in the 3′ UTR (3′ UTR-APA) is a mode of gene expression regulation, fundamental for mRNA stability, translation and localization. In the immune system, it was shown that upon T cell activation, there is an increase in the relative expression of mRNA isoforms with short 3′ UTRs resulting from 3′ UTR-APA. However, the functional significance of 3′ UTR-APA remains largely unknown. Here, we studied the physiological function of 3′ UTR-APA in the regulation of Myeloid Cell Leukemia 1 (*MCL1*), an anti-apoptotic member of the Bcl-2 family essential for T cell survival. We found that T cells produce two *MCL1* mRNA isoforms (pA1 and pA2) by 3′ UTR-APA. We show that upon T cell activation, there is an increase in both the shorter pA1 mRNA isoform and MCL1 protein levels. Moreover, the less efficiently translated pA2 isoform is downregulated by miR-17, which is also more expressed upon T cell activation. Therefore, by increasing the expression of the more efficiently translated pA1 mRNA isoform, which escapes regulation by miR-17, 3′ UTR-APA fine tunes MCL1 protein levels, critical for activated T cells' survival. Furthermore, using CRISPR/Cas9-edited cells, we show that depletion of either pA1 or pA2 mRNA isoforms causes severe defects in mitochondria morphology, increases apoptosis and impacts cell proliferation. Collectively, our results show that *MCL1* alternative polyadenylation has a key role in the regulation of MCL1 protein levels upon T cell activation and reveal an essential function for *MCL1* 3′ UTR-APA in cell viability and mitochondria dynamics.

Keywords Alternative polyadenylation · 3′ UTR · T lymphocytes · Gene Regulation · *MCL1*

Introduction

Approximately 70% of all human genes produce mRNAs with distinct 3′ ends due to the usage of multiple polyadenylation signals (PASs), contributing to transcriptome diversity [1–3]. This widespread mechanism, known as alternative polyadenylation (APA), has emerged as an important mode of co-transcriptional gene regulation, being fundamental for mRNA localization, stability, translation efficiency, and protein subcellular localization [2, 4–6]. When APA is restricted to the 3′ untranslated region (3′ UTR-APA), it originates mRNA isoforms that differ in the length of their 3′ UTR, yet encode the same protein [5, 7]. The 3′ UTR is a central hub for gene expression regulation,

Beatriz C. Garcia and Ana Curinha contributed equally to this work.

✉ Isabel Pereira-Castro
isabel.castro@ibmc.up.pt

✉ Alexandra Moreira
alexandra.moreira@i3s.up.pt

[1] Gene Regulation, i3S, Instituto de Investigação E Inovação Em Saúde, Universidade Do Porto, Porto, Portugal

[2] Gene Regulation, IBMC, Instituto de Biologia Molecular E Celular, Universidade Do Porto, Porto, Portugal

[3] Instituto Gulbenkian de Ciência (IGC), Oeiras, Portugal

[4] i3S, Instituto de Investigação E Inovação Em Saúde, Universidade Do Porto, Porto, Portugal

[5] INEB, Instituto de Engenharia Biomédica, Universidade Do Porto, Porto, Portugal

[6] ICBAS, Instituto de Ciências Biomédicas Abel Salazar, Universidade Do Porto, Porto, Portugal

[7] Present Address: Department of Molecular Biology and Genetics, John Hopkins University School of Medicine, Baltimore, MD, USA

containing *cis*-regulatory sequences such as microRNA (miRNA) target sites and RNA-binding protein (RBP) binding sites [5, 8]. Longer 3′ UTRs are more prone to regulation because they contain more miRNAs and RBPs *cis*-regulatory sequences than shorter 3′ UTRs [9, 10]. The 3′ UTR contains the PAS that defines the pre-mRNA 3′ end processing and the polyadenylation site. The PAS is generally located 10–35 nucleotides upstream of the cleavage site, and consists of the canonical AAUAAA hexamer sequence or a similar weaker variant [11, 12]. Additional auxiliary *cis*-elements, localized upstream (USE) and downstream (DSE) of the PAS, are often needed to enhance the selection of weaker PAS [13–16]. Selection of the PAS is also dictated by polyadenylation factors and other protein factors [2, 17, 18]. Therefore, the site and efficiency of polyadenylation depends on both *cis*- and *trans*- acting factors, and small differences in the intracellular concentrations of these factors have the potential to affect the choice of one PAS over another [17, 19–22].

Several transcriptomic studies have identified specific APA patterns associated with disease, proliferation and differentiation conditions (reviewed in [2, 23, 24]). Globally, activated T cells [25], activated hematopoietic stem cells [26], macrophages responding to infection [27], cancer cells [28, 29] and differentiated syncytiotrophoblasts [30] produce mRNAs with shorter 3′ UTRs, allowing them to escape regulation by RBPs or miRNAs, specifically targeting isoforms with longer 3′ UTRs. In contrast, there is a preferential usage of distal PASs resulting in mRNAs with longer 3′ UTRs, and thus more prone to undergo post-transcriptional regulation, during cellular senescence [31], development [9] and in neuronal tissues [10, 32]. Although these studies catalogue the global APA patterns for certain physiological conditions or disease, they do not elucidate in detail the mechanisms of APA regulation and the functional relevance of the 3′ UTR-APA isoforms in individual genes. In this regard, some studies have shown that 3′ UTR-APA isoforms can indeed have physiologically relevant functions. In particular, we have shown that *CD5* is regulated by 3′ UTR-APA to fine-tune CD5 protein expression in activated human T cells [33], that the longer 3′ UTR of *Rac1* plays an essential role in neurite outgrowth [34], and that the longest 3′ UTR variant of *polo* is vital for the production of this protein and *Drosophila* histoblast proliferation [35]. Moreover, others have shown that *Pax3* alternative 3′ UTRs control muscle stem cell fate and muscle function [36], that the *BDNF* long 3′ UTR has a role in *BDNF* mRNA trafficking and dendritic functioning in hippocampal neurons [37], and a role for *CD47* alternative 3′ UTRs in CD47 protein localization has been uncovered [4]. It is clear from these studies that 3′ UTR-APA mRNA isoforms possess important biological functions, but their regulation and function remain poorly investigated by single gene studies.

In this study, we investigated the function of Myeloid Cell Leukemia 1 *(MCL1)* 3′ UTR-APA and its expression regulation in human T cells. We focused on MCL1 because it plays a critical role for the survival of T cells throughout their development and maintenance [38]. MCL1 is a member of the B cell lymphoma-2 (Bcl-2) family of apoptosis regulators with a well described anti-apoptotic function required for the survival of multiple cells, in particular for those of the hematopoietic lineage [39–41]. MCL1 is constitutively expressed during all developmental stages of T lymphocytes and plays an essential function in their survival and maintenance, in particular in naïve and activated T lymphocytes [38, 42]. In addition to its anti-apoptotic function, MCL1 contributes to autophagy, mitochondrial homeostasis, regulation of protein kinase signaling and to nuclear events related to cell cycle control (reviewed in [41]). However, the biological relevance of MCL1 non-apoptotic functions has not been extensively studied.

MCL1 was initially shown to be overexpressed in a human myeloblastic leukemia cell line at early stages of differentiation and MCL1 upregulation was observed in many cancers [38, 39, 41]. MCL1 is overexpressed in B- and T-lineage non-Hodgkin lymphomas [43] and in solid tumors, including breast cancer [44], lung cancer [45], and hepatocellular carcinoma [46], among others [41]. Of note, this increased expression is associated with poor-prognosis [43, 45, 46]. Considering that MCL1 plays a major role in apoptosis suppression, counteracting MCL1 function may be used as a strategy in anti-cancer therapies. In fact, MCL1 inhibitors are already being tested in Phase I clinical trials [41]. Consequently, studies expanding our understanding on how *MCL1* expression is regulated will contribute to explore their therapeutic potential in cancer and immune conditions.

In summary, we found that *MCL1* produces two mRNA isoforms, the short pA1 mRNA isoform and the long pA2 mRNA isoform by 3′ UTR-APA, that are independent from alternative splicing. Upon cell activation, there is an increase in the expression of the short pA1 mRNA isoform correlating with an increase in MCL1 protein levels, vital for the survival of activated T cells. We show that miR-17 binds to pA2 mRNA isoform and thus fine tunes MCL1 protein expression as this mRNA isoform is less efficiently translated. Furthermore, our results show that alternative polyadenylation of *MCL1* is essential as both *MCL1* 3′ UTR-APA mRNA isoforms are essential for MCL1 function in cell viability and for mitochondria morphology.

Materials and methods

In silico analysis

MCL1 reference sequences from human and nine other mammalian species were obtained from the Ensembl and NCBI Nucleotide databases. The sequences were aligned using the default settings of the MUSCLE software running on Geneious v5.5.6 [47] to determine the conservation on 3′ UTR and miRNAs putative-target sites. The identification of miRNAs that putatively target *MCL1* was performed using the default settings of the TargetScan (http://www.targetscan.org/), microRNA (http://www.microRNA.org/), miRbase (http://www.mirbase.org/search.shtml) and miRTarBase (http://mirtarbase.mbc.nctu.edu.tw/) databases. The microRNA and miRNAmap (http://mirnamap.mbc.nctu.edu.tw/) databases were used to determine expression of the miRNAs in T cells.

Human PBMCs and primary T cell isolation and activation

Human buffy coats were obtained from healthy blood donors from Serviço de Imunohemoterapia, Hospital de São João (Porto, Portugal), and was approved by the Centro Hospitalar Universitário São João Ethics Committee (protocol 90/19), after each donor informed consent collection. Peripheral blood mononuclear cells (PBMCs) were isolated from the buffy coats using Lympholyte-H (Cedarlane Labs) according to the manufacturer's instructions. Human primary T cells were isolated from PBMCs using the EasySep Human T Cell Enrichment Kit (StemCell Technologies) following the manufacturer's protocol. After isolation, PBMCs and T cells were maintained in Roswell Park Memorial Institute (RPMI) 1640 medium with GlutaMAX (Thermo Fisher Scientific), supplemented with 10% heat-inactivated fetal bovine serum (FBS) (Thermo Fisher Scientific), 100 U/mL penicillin and 100 µg/mL streptomycin antibiotic solution (Thermo Fisher Scientific). Human PBMCs and primary T cells were activated with phytohemagglutinin (PHA-P; Sigma) at a final concentration of 10 µg/mL for 24 h.

Cell culture

The Jurkat E6.1 cell line was cultured in RPMI 1640 medium with GlutaMAX. HeLa, NIH3T3 and 293T cell lines were cultured in Dulbecco's Modified Eagle Medium (DMEM) with GlutaMAX (Thermo Fisher Scientific) and HAP1 cells in Iscove's Modified Dulbecco's Medium (IMDM) (Thermo Fisher Scientific). All cell lines were supplemented with 10% heat-inactivated FBS, 100 U/mL penicillin and 100 µg/mL streptomycin antibiotic solution, maintained in a humidified incubator at 37 ºC with 5% CO_2, and subcultured every 3 days.

Actinomycin D treatment

Resting or activated Jurkat E6.1 cells (1×10^6 cells) were cultured in 24-well plates in RPMI 1640 medium supplemented with 10% heat-inactivated FBS, and treated with 5 µg/mL of Actinomycin D (Sigma) for 0.5, 1, 2, 4 and 6 h. No Actinomycin D was added to the cells in the 0 h time point. Cells were maintained in a humidified incubator at 37 °C with 5% CO_2 through the course of the experiment. At the end of each time point, cells were resuspended in 1 mL TRIzol Reagent (Thermo Fisher Scientific) for RNA extraction.

RNA extraction

Total RNA was extracted using TRIzol Reagent following the manufacturer's standard protocol, with the exception that all RNA precipitations were carried out at – 80 °C, during at least 2 h, and using 1 µL of glycogen (15 mg/mL; Thermo Fisher Scientific). DNase I treatment of total RNA was performed using 10 U of DNase recombinant I (Roche) in a final volume of 12 µL. Samples were incubated at 37 °C for 30 min followed by 10 min at 75 °C for enzyme inactivation. Total RNA enriched with miRNAs was extracted using the mirVana miRNA Isolation Kit (Thermo Fisher Scientific) according to the manufacturer's instructions with minor modifications. Briefly, the washing step with miRNA Wash Solution 1 was separated in two steps performing the DNase I treatment (final concentration 3 U/µL) in between. RNA quantification was performed using the NanoDrop 1000 Spectrophotometer (Thermo Fisher Scientific) and the RNA stored at – 80 ºC.

cDNA synthesis

For gene expression analyses, cDNA was synthesized from 500 ng or 1000 ng of total RNA (previously treated with DNase I) using SuperScript IV Reverse Transcriptase (Thermo Fisher Scientific), according to the manufacturer's protocol. To rule out genomic DNA contamination, a mixture without reverse transcriptase was also prepared. For miRNA expression analyses, cDNA was synthesized from

10 ng of total RNA enriched with miRNAs using the Multiscribe Reverse Transcriptase (Thermo Fisher Scientific) and the RT primer (Thermo Fisher Scientific), according to the manufacturer's protocol.

Reverse transcription quantitative real-time PCR (RT-qPCR)

RT-qPCRs were prepared using 1 µL of cDNA and 9 µL of a mixture containing 5 µL of SYBR Select Master Mix (Applied Biosystems), 0.125 µL (0.125 µM) of each primer (listed in Supplementary Table S1) and 3.75 µL of nuclease-free water. Samples were run in triplicate on a 7500 Fast Real-Time PCR System (Applied Biosystems), using the 60 ºC default program recommended by the manufacturer. Real-time PCR primer efficiencies were calculated from the slope obtained by the serial dilutions using the equation: $E = 10^{[-1/slope]}$ [48]. Results were analyzed using the ΔC_t method (Relative expression) or the $\Delta\Delta C_t$ method (Normalized fold expression) using *18S* or *GAPDH* reference genes to normalize the gene expression [48]. For miRNA expression quantification, reactions were prepared by including 10 µL of TaqMan Universal PCR Master Mix II (Applied Biosystems), 1 µL of 20X TaqMan Small RNA Assay (Applied Biosystems), 1.3 µL of cDNA and nuclease-free water up to 20 µL. The final reaction mixtures were run in a StepOne Real-time PCR System (Applied Biosystems) using the 60 °C default program. Results were analyzed applying the ΔC_t method [48] and using the human U6 small nuclear RNA as reference gene.

3′ Rapid amplification of cDNA ends (3′ RACE)

The SMARTer RACE cDNA Amplification kit (Clontech) was used to synthesize 3′ RACE cDNA, using the SMARTScribe Reverse Transcriptase and 1 µg of total RNA, according to the manufacturer's protocol. The 3′ RACE PCRs were prepared using the Phusion High-Fidelity DNA Polymerase (Thermo Fisher Scientific) following the manufacturer's protocol. The forward gene-specific primers were designed according to the SMARTer RACE kit guidelines (primers listed in Supplementary Table S1). The PCR products were analyzed by 1.5% agarose gel electrophoresis and purified using the QIAquick Gel Extraction Kit (QIAGEN). Purified PCR products were cloned into a pCR2.1-TOPO vector using the TOPO-TA Cloning® Kit (Thermo Fisher Scientific), according to the manufacturer's protocol. Plasmid DNA was extracted using PureLink Quick Plasmid Miniprep Kit (Thermo Fisher Scientific) and sequenced on a 3500 Genetic Analyzer sequencer (Applied Biosystems) to map the mRNAs 3′ ends.

Northern blot

Northern blot was performed using the DIG DNA Labelling and Detection Kit (Roche). The DNA probes targeting *MCL1* and *ACTB* coding sequences were prepared by PCR (primers listed in Supplementary Table S1) and labeled with digoxigenin (DIG) according to the manufacturer's instructions. The efficiency of DIG-labeled probes was determined by comparing the probes with a series of dilutions of a control DIG-labeled DNA, following the manufacturer's protocol. RNA samples (20 µg) were denatured and separated by electrophoresis on a 1% formaldehyde agarose gel, with a DIG-labeled RNA molecular weight marker II (Roche), for 5–6 h at 90 V. Separated RNAs were transferred overnight by capillary transfer onto a positively charged nylon membrane (GE Healthcare) and the membrane was UV-crosslinked on a UVC 500 Crosslinker (Hoefer). The RNA blot was hybridized with the DIG-labeled probe overnight under agitation at 42 °C in a hybridization oven. Detection was made using the anti-digoxigenin antibody conjugated to alkaline phosphatase and the DIG Detection Kit (Roche), according to the manufacturer's guidelines. Northern blot visualization was performed in the ChemiDoc XRS + System (Bio-Rad).

Western blot

Whole-cell protein extracts were obtained via cell lysis with NP-40 cell lysis buffer (50 mM Tris–HCl pH 8.0, 150 mM NaCl, 1% NP-40), supplemented with 1X protease inhibitors (Sigma). Protein extracts (25 µg) were resolved on a 10% SDS-PAGE and transferred into a nitrocellulose membrane using the iBlot Gel Transfer Device (Thermo Fisher Scientific). The membrane was incubated with primary antibodies diluted in TBS-0.1% Tween 20 containing 5% non-fat dried milk, followed by three washes with TBS-0.1% Tween 20 and incubation with the appropriate secondary antibody. The antibodies used were: anti-human MCL1 mouse monoclonal antibody (Ab22; eBioscience, 1:750 dilution), anti-α-tubulin mouse monoclonal antibody (B-5-1-2; Sigma, 1:100,000 dilution), anti-heat shock cognate 70 (HSC70) mouse monoclonal antibody (sc-7298; Santa Cruz Biotechnologies, 1:1000 dilution), goat anti-rabbit IgG-HRP secondary antibody (Santa Cruz Biotechnologies) and goat anti-mouse IgG-HRP secondary antibody (Santa Cruz Biotechnologies). Detection was achieved using enhanced chemiluminescence (ECL Prime, GE Healthcare) and the immunoblots were visualized on the ChemiDoc XRS + System (Bio-Rad). Quantification of the protein intensity was performed on Image lab Software (Bio-Rad).

Plasmids

Luciferase reporter plasmids were made by amplification of the 3′ UTR from *MCL1* pA1 and pA2 mRNA isoforms using as template the 3′ RACE sequences cloned into the pCR2.1-TOPO vector, and forward and reverse primers with *Sac*I and *Sal*I restriction sites, respectively. Amplifications were performed for 25 cycles at 56 °C using Phusion High-Fidelity DNA Polymerase (Thermo Fisher Scientific), following the manufacturer's instructions. Amplified PCR products were purified using the QIAquick PCR Purification Kit (QIAGEN). PCR products were digested with *Sac*I and *Sal*I restriction enzymes (New England Biolabs) and cloned downstream of a luciferase reporter gene in an in-house luciferase plasmid pLuc [33] digested with the same enzymes. The luciferase reporter constructs were named pLuc-pA1 and pLuc-pA2. In the pLuc-pA2 plasmid, mutation of the proximal polyadenylation signal (PAS1) was performed by site-directed plasmid mutagenesis using the primers listed in Supplementary Table S1 and the protocol described in [49]. Mutations in miR-92a, miR-29b, miR-17 and miR-320a target sites were also performed in the pLuc-pA2 plasmid by site-directed plasmid mutagenesis. The constructs were then used as PCR templates to clone the mutated miRNAs target sites and flanking regions (~ 100 bp) into the pmirGLO vector (Promega) in *Sac*I and *Sal*I restriction sites. Again, the primers used to amplify these sequences contained the *Sac*I (forward) and *Sal*I (reverse) restriction sites at their 5' end. The miRNA wild-type target sequences were amplified using pLuc-pA2 as template and cloned into pmirGLO in *Sac*I/*Sal*I restriction sites as described above. The *Renilla* plasmid pRL-TK (Promega) was used for luciferase activity normalizations. The pcDNA3-miR-17 expression plasmid used for miR-17 overexpression was a gift from Joshua Mendell (Addgene plasmid #21113) [50]. EGFP-MCL1 fused constructs used for confocal microscopy were made by amplification of the *MCL1* coding sequence (CDS) using Jurkat E6.1 cDNA and primers containing *Bgl*II and *Sac*I cloned into the pEGFP-C1 (Clontech), digested with the same restriction enzymes. The MCL1-pA1 and MCL1-pA2 constructs were made by digestion of the 3′ UTRs of pLuc-pA1 and pLuc-pA2 with *Sac*I/*Sal*I and cloning into MCL1-CDS using the same enzymes. The primer sequences used for plasmid constructions are listed in Supplementary Table S1. Plasmid DNA extractions were performed using the ZR Plasmid Miniprep kit (ZYMO Research) according to the manufacturer's protocol. All plasmids were sequenced on an ABI 3130XL Automated Sequencer (Applied Biosystems) to confirm that they had been accurately constructed.

Transfections

HeLa or NIH3T3 cells were seeded on 24-well plates and transfected at 70–90% confluency using Lipofectamine 2000 (Thermo Fisher Scientific) or jetPRIME (Polyplus-transfection) transfection reagents, according to the manufacturers' protocols. Jurkat E6.1 cells were transfected by nucleofection using the Amaxa Cell line Nucleofactor kit V (Lonza), using the X-005 manufacturers' protocol for E6.1 cells. Transfections were performed using a total of 0.5 µg of plasmid DNA for lipofections or 2 µg for nucleofections. In the Luciferase activity experiments, co-transfected plasmids were divided as follows: 0.35 µg for pLuc-pA1 or pLuc-pA2 plasmids and 0.15 µg for pRL-TK *Renilla* plasmid in the case of lipofections and 1.5 µg for pLuc-pA1 or pLuc-pA2 plasmids and 0.5 µg for pRL-TK *Renilla* plasmid in nucleofections. For the miRNA/plasmid co-transfection we used 0.5 µg (for NIH3T3 cells) or 2 µg (for Jurkat E6.1) of pmiRGlo plasmids and 50 nM (for NIH3T3) or 300 nM (for Jurkat E6.1) of a MISSION hsa-miR-17 Mimic (Sigma) or a miRNA Negative Control (Sigma). In all experiments, cells were harvested 48 h post-transfection.

Luciferase assays

Luciferase assays were performed using the Dual-Luciferase Reporter Assay System (Promega) according to the manufacturer's guidelines. Briefly, Jurkat E6.1, HeLa or NIH3T3 cells were harvested and rinsed once with 1X PBS. Then, 100 µL of 1X Passive Lysis Buffer was added followed by 15 min shaking at room temperature. 10 µL of each sample was placed on a 96-well black plate (Costar) and 50 µL of LAR II was added to perform the measurement of the firefly luciferase activity. Next, 50 µL of Stop & Glo Reagent was added to each condition to perform the *Renilla* luciferase activity measurement. Luminescent measurements of both firefly and *Renilla* luciferase activities were performed in a Synergy 2 Multi-Mode Reader (Bio-Tek). Firefly luciferase activity was normalized to the *Renilla* luciferase activity.

Generation of *MCL1* ΔpA1 and ΔpA2 CRISPR/Cas9 cell lines

Cells without pA1 or pA2 mRNA isoforms (*MCL1* ΔpA1 and ΔpA2) were made by deletion of the PAS1 or PAS2 polyadenylation signals by genome editing using CRISPR/Cas9 lentivirus constructs. Briefly, single guide RNAs (sgRNAs) flanking PAS1 or PAS2 were designed in the CRISPR Design online software (http://crispr.mit.edu/). Annealed sgRNA oligos (Supplementary Table S2) were

cloned into the lentiCRISPR v2 (Addgene plasmid #52961 [51]; a gift from Feng Zhang) or lentiCRISPR v2-Blast (Addgene plasmid #83480; a gift from Mohan Babu) all-in-one plasmids according to the Zhang Lab protocol [51]. Lentiviral particles for each lentiCRISPRv2-sgRNA construct were produced in the 293T packaging cell line transfected with the respective lentiCRISPRv2 sgRNA construct along with pCMV-dR8.91 and pMD2.G plasmids (2 µg of total DNA in equimolar ratios) in 6-well plates and using jetPRIME transfection reagent. Media was changed 4 h later, and 48 h after transfection the lentivirus-containing media was harvested and filtered through a 0.45 µm filter. Afterwards, 2 mL of media containing the lentiviral particles (1 mL of each sgRNAs flanking either PAS1 or PAS2) and 8 µg/mL of polybrene were added to Jurkat E6.1, Hela and HAP1 cells for 24 h in 6-well plates. Stably infected cells were selected 72 h post-transduction using 5 µg/mL puromycin in the case of Jurkat E6.1 cells, 3 µg/mL of puromycin in HeLa cells and 2 µg/mL of puromycin plus 5 µg/mL of blasticidin in HAP1 cells. Single-cell clones were isolated from the CRISPR bulk populations by single cell sorting into 96-well plates using the FACS Aria II Cell Sorter (BD Biosciences). DNA from bulk populations or single cell populations was extracted using a phenol:chloroform:isoamyl alcohol protocol, and genotyped by PCR using primers flanking the deletions (Supplementary Table S1).

Flow cytometry

The Annexin V-Propidium Iodide staining of Jurkat E6.1 and HeLa cells for flow cytometry analysis was performed using the FITC Annexin V Apoptosis Detection Kit I (BD Biosciences) following the recommended procedure. In HeLa cells, the supernatant media was centrifuged together with the trypsinized cells at 300 g for 5 min. Mono-label cells with Propidium iodide or Annexin V and unstained cells were used as controls. Proliferation assay was performed using the CellTrace™ Violet Cell Proliferation Kit (Thermo Fisher Scientific) following the recommended procedure. Briefly, 3×10^5 cells per condition were stained with CTV at day 0 and incubated for 72 h following staining. A CTV positive control was prepared on the day of the analysis for the non-proliferation control. Cells without CTV staining were used as the unstained population. Cell cycle analysis was performed using 5×10^5 cells per condition. Briefly, cells were trypsinized and washed with cold PBS, centrifuged at 300 g for 5 min and resuspended in 700 µL of PBS. Cells were fixed in 1400 µL of cold absolute ethanol added drop-wise with gentle vortexing and kept at − 20 °C for at least 2 h. Cells were then resuspended in 10 mL of PBS, centrifuged at maximum speed and the supernatant removed. A mixture containing 25 µL of Propidium iodide (1 mg/mL in water, Invitrogen), 5 µL of RNaseA (10 mg/mL, Sigma) and 470 µL of PBS was added to the cell pellet followed by incubation in the dark at 37 °C for 30 min. The cell cycle profile was determined for 10,000 events per sample. Filtered cells were analyzed on a BD FACS Canto II (BD Biosciences) flow cytometer and the results were obtained and analyzed with the FlowJo v10 software (Becton, Dickinson and Company).

Confocal microscopy

For mitochondrial labeling, HeLa cells transfected with the EGFP-MCL1 fused constructs were incubated at 37 °C for 30 min with 50 nM of MitoTracker™ CMXRos Red (Thermo Fisher Scientific) diluted in DMEM medium in a 5% CO_2 humidified incubator. Nuclear staining was performed with 1 µg/mL of Hoechst 33342 dye (Thermo Fisher Scientific) for 15 min at 37 °C in a 5% CO_2 humidified incubator. Cells were washed three times with 1X PBS between all incubations. Live cell microscopy images were acquired on a Leica TCS SP5 confocal microscope (Leica Microsystems), using the 63X oil objective, and the 405 nm (Hoechst), 488 nm (EGFP-MCL1 fused constructs) and 561 nm (MitoTracker™ Red) laser sets. In each individual experiment, microscope settings were the same between the different conditions (e.g., laser intensity, zoom, and signal gain). Images were processed and analyzed using the Fiji ImageJ software [52].

Mitochondria morphology analysis

Live cell imaging was performed in cells previously stained with 50 nM of MitoTracker Red CMXRos (Thermo Fisher Scientific) and 1 µg/mL of Hoechst 33342 dye (Thermo Fisher Scientific). Images were acquired on a Leica TCS SP5 confocal microscope (Leica Microsystems), using the 63X oil objective, and the 405 nm (for Hoechst), and 561 nm (for MitoTracker Red) lasers. In each individual experiment the microscope settings were the same between the different conditions.

The image analysis workflow consisted on three stages: (a) mitochondria segmentation and classification, (b) nuclei segmentation, and (c) extraction of relevant data. On the first stage, mitochondria was segmented and classified using a combination of standard image analysis operations (implemented on ImageJ/Fiji [52, 53]) and machine learning algorithms (implemented on ilastik [54]). In short, raw images

were pre-processed by applying a Difference of Gaussians filter (Fiji's plugin CLIJ2 [55–57]) with sigmas 1.5 and 2 to smooth image noise and enhance structures compatible to the mitochondrial size. Then, machine learning algorithms were used first to segment mitochondria, and later to classify each of the detected objects into one of three possible mitochondria subtypes/classes: puncta (small round objects), rods (elongated objects) and networks (elongated objects with agglomerations). For the segmentation workflow, features focusing on (a) pixel intensity—such as Gaussian smoothing, (b) edges—such as Laplacian of Gaussian, Gaussian gradient magnitude or difference of Gaussians, or (c) texture—such as structure tensor eigenvalues or Hessian of Gaussian eigenvalues, were computed for a set of pixels manually annotated as either mitochondria or background. Then, a random forest classifier [58] was trained to predict mitochondria segmentation. After segmentation, touching mitochondria were split using a marker-controlled watershed algorithm, and a set of them was manually annotated as belonging to one of the three considered classes (puncta, rods or network). Shape features—such as size, principal components or radii of the objects, convex Hull features—such as convexity, number of defects, convex Hull area or object area, and skeleton features—such as average branch length or number of branches, were computed for each annotated object to train a second classifier capable of distinguish between the three classes.

The second stage of the workflow focused on the segmentation of nuclei. After the application of a Gaussian blur (sigma = 5) to smooth the image, and a 1/2 rescale factor, the deep learning algorithm StarDist 2D [59] was applied to segment nuclei. The resulting segmented image was then scaled back to the size of the original image and post processed to remove small particles.

Finally, the results of the previous steps were combined to compute statistics of mitochondria and the distance between mitochondria and nuclei using Fiji's 3D Image Suite plugin [60]. The described workflow as well as the training datasets used can be downloaded from: https://github.com/econdesousa/ImageAnalysis/tree/master/MitochondrialStats.

2D intensity measurements

For the fluorescence intensity quantifications, a workflow was mainly developed in ImageJ macro language (implemented in the Fiji distribution v1.53n) [52] with the cell segmentation performed with cellpose [61] and is available at https://github.com/econdesousa/CellPoseSegPlusIntensityMeasurement. For each image, the green signal channel (488 nm) was extracted and saved to a png file format. Then, each png file was uploaded to https://www.cellpose.org/ to get the corresponding segmentation by asking cellpose to segment cytoplasms of diameter 60 pixels by considering grayscale images without nuclei channel.

After this manual step, an ImageJ macro-script was developed to open the original image, extract the signal channel, and subtract the background (rolling ball algorithm with radius 50 pixels). Then, the cellpose corresponding mask was open, converted to a 16-bit grayscale image, and relabelled with command closeIndexGapsInLabelMap of CLIJ2 plugin [57]. Finally, the resulting labeled image and the background-subtracted signal channel were used to quantify the fluorescence intensity with the command Intensity Measurements 2D/3D of MorpholibJ plugin [62].

Statistical analysis

Data are presented in the graphs as mean ± SD (standard deviation) and are from at least three independent experiments. Statistical differences were tested using two-tailed unpaired or paired *t* test, one-way ANOVA or 2-way ANOVA, as appropriate. *P* values below 0.05 were considered statistically significant. Information regarding the applied statistical analysis and significant *p* values can be found in the figure legend of the respective figure. All graphs were made using GraphPad Prism version 6.01 (GraphPad Software).

Results

MCL1 undergoes 3′ UTR-APA that is independent from alternative splicing in T cells

A significant number of genes change their expression profile during T cell activation, displaying shorter 3′ UTRs that correlate with cell proliferation [25]. We focused our study on *MCL1* as it stands out as an essential gene for T cell development, maintenance and survival [38, 42]. We used human healthy donors to isolate primary T cells and used an established ex vivo model to study resting and activated T cells (Fig. 1a). By 3′ RACE mapping and sequencing, we identified two distinct *MCL1* mRNA isoforms (named pA1 and pA2 mRNA isoforms) (Fig. 1b) that differ in their 3′ UTRs (1420 and 2818 nucleotides long, respectively, Supplementary Fig. S1a), due to the differential usage of two PAS. *MCL1* 3′ UTR conservation analysis shows that the 3′ UTR possess an overall pairwise identity of 65.5% in the ten mammalian species analyzed (Fig. 1c). Notably, both pA1 and pA2 mRNA isoforms use canonical PASs (AAUAAA) that are highly conserved in mammals: PAS1 is 97% and PAS2 is 100% conserved (Fig. 1c). The high degree of 3′ UTR conservation and PASs similarity prompted us to investigate the physiological function of the two mRNA isoforms produced by *MCL1* 3′ UTR-APA. Expression levels of pA1 and pA2 mRNAs were quantified

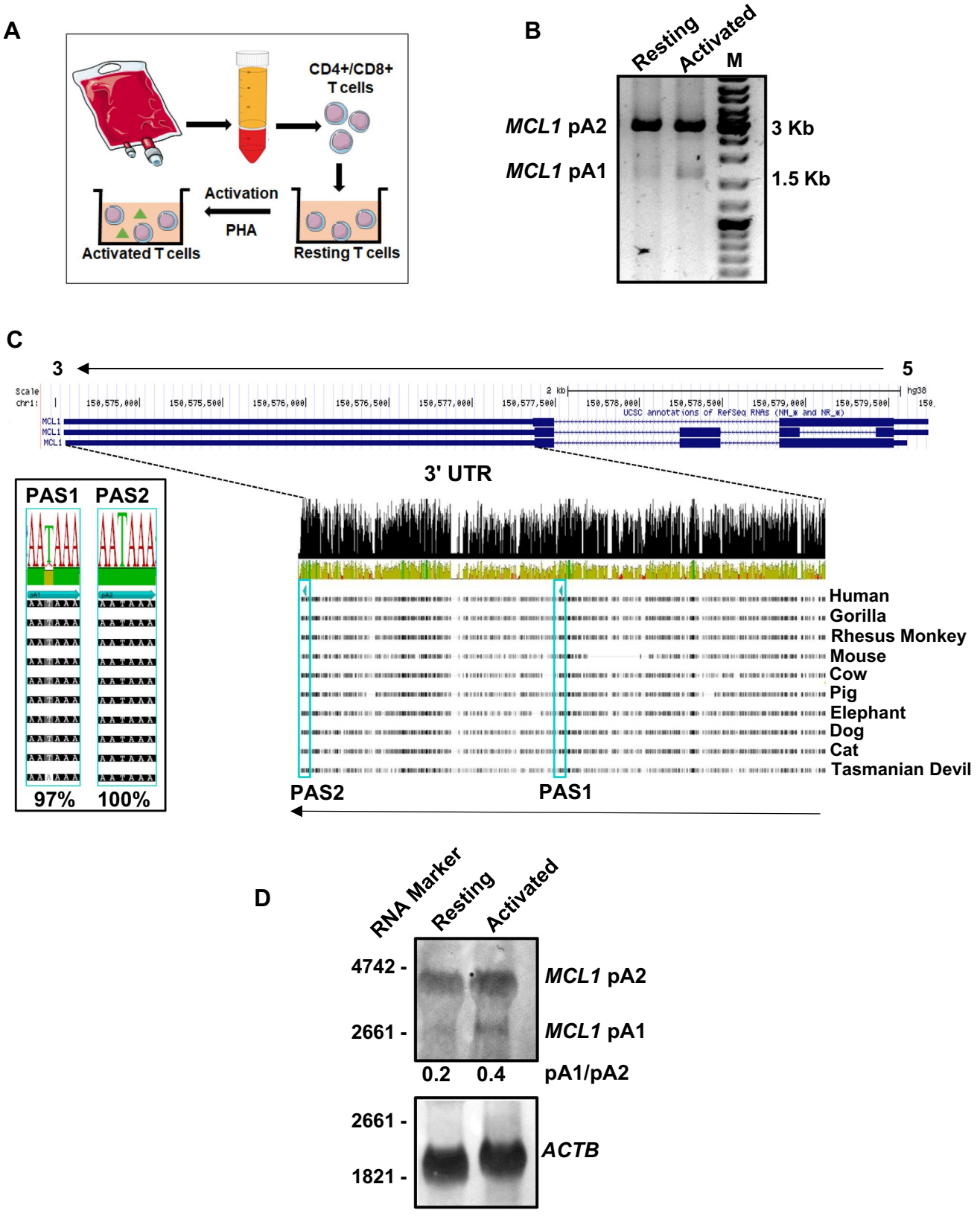
A
CD4+/CD8+
T cells
Activation
PHA
Activated T cells
Resting T cells
B
Resting
Activated
M
MCL1 pA2
MCL1 pA1
3 Kb
1.5 Kb
C
3
5
3' UTR
PAS1
PAS2
97%
100%
Human
Gorilla
Rhesus Monkey
Mouse
Cow
Pig
Elephant
Dog
Cat
Tasmanian Devil
PAS2
PAS1
D
RNA Marker
Resting
Activated
4742 -
2661 -
MCL1 pA2
MCL1 pA1
0.2
0.4
pA1/pA2
2661 -
1821 -
ACTB

◂**Fig. 1** *MCL1* undergoes 3′ UTR-APA generating pA1 and pA2 mRNA isoforms that are conserved in mammals. **A** The experimental setup used in this work. Primary T cells or PBMCs were isolated from buffy coats of healthy blood donors and maintained in a naïve state (resting) and activated using PHA. **B** Representative image of a 3′ RACE showing that *MCL1* produces two alternative mRNAs (pA1 and pA2) in resting and activated human primary T cells. **C** The polyadenylation signals of *MCL1* pA1 and pA2 mRNA isoforms located in the 3′ UTR are highly conserved in mammals. Above, snapshot of the *MCL1* locus retrieved from the UCSC Genome Browser database (http://genome.ucsc.edu/). The genome orientation is indicated by the arrows. Below, multiple sequence alignment of the *MCL1* 3′ UTR in ten representative mammalian species reveals high conservation throughout the whole 3′ UTR sequence. The PASs are indicated by blue arrows and rectangles. Sequence identity (green and red bars) and logos (black) are shown above the alignment. A snapshot of the two PAS alignment with sequence identity, logos and pairwise percent identity is shown on the left. **D** Northern blot confirms the expression of the two *MCL1* mRNA isoforms in T cells. Overall, the longer pA2 mRNA is more expressed than the pA1 mRNA but upon cell activation pA1 mRNA expression increases ~ twofold. *ACTB* was used as a loading control. Molecular weight was determined using a DIG-labeled RNA marker. pA1/pA2 ratio is shown below the *MCL1* northern blot and in Supplementary Fig. S1b, $n = 1$

by Northern blot (Fig. 1d), revealing that the pA2 mRNA isoform is more expressed than the pA1 mRNA in both resting and activated conditions. We also observed that cell activation correlates with a twofold increase in the expression of the short pA1 mRNA isoform (Fig. 1d and Supplementary Fig. S1b), in agreement with previous APA transcriptomic analyses [25]. This corresponds to a twofold increase in the pA1/pA2 mRNA isoform ratio upon cell activation (Fig. 1d).

It is well established that *MCL1* undergoes alternative splicing producing long (*MCL1L*) and short (*MCL1S*) mRNAs that are determinant for MCL1 protein function. *MCL1L* is responsible for the characteristic anti-apoptotic function of MCL1 [63], while *MCL1S* is pro-apoptotic [64]. To evaluate the contribution of alternative splicing in the two 3′ UTR-APA mRNAs, we used specific primers for each alternative splicing mRNA isoform and mapped the mRNAs 3′ ends by 3′ RACE. We found that *MCL1L* and *MCL1S* mRNAs have the same 3′ ends (Fig. 2a). Four mRNA isoforms were thus identified in T cells (Fig. 2b): *MCL1L-pA1, MCL1L-pA2, MCL1S-pA1 and MCL1S-pA2*. These results indicate that the *MCL1* alternative polyadenylation event is independent of alternative splicing. We then quantified *MCL1L* and *MCL1S* expression in human primary T cells and observed that the canonical *MCL1L* is 70-fold more expressed than *MCL1S* (Fig. 2c). Given that *MCL1S* is poorly expressed in T cells, we thus focused our 3′ UTR-APA study on *MCL1L*.

Shortening of *MCL1* 3′ UTR upon T cell activation correlates with an increase in MCL1 protein levels

We next quantified by RT-qPCR *MCL1* pA1 and pA2 mRNAs expression levels in resting and activated primary T cells isolated from five human blood healthy donors. Human primary T cells stimulated for 24 h with PHA were confirmed to be in an activated state by measuring the expression levels of the CD69 activation marker (Supplementary Fig. S1c). In the RT-qPCR, we used a primer pair (pA1 + pA2) that hybridizes to the *MCL1* coding sequence (CDS) and thus amplifies both pA1 and pA2 mRNA isoforms and a primer pair (pA2) that is specific for the longest pA2 mRNA, as previously described [19, 34, 35]. Primer pair efficiencies can be found in Supplementary Fig. S1d. After T cell activation, we observed an increase in the expression of *MCL1* pA1 + pA2 mRNAs but not in *MCL1* pA2 mRNA (Fig. 3a). This result agrees with our 3′ RACE and Northern blot data showing that upon T cell activation only the short pA1 mRNA levels increase (Fig. 1b and d). To evaluate if this increase was due to mRNA stability differences, we treated resting and activated Jurkat E6.1 cells with actinomycin D and determined *MCL1* mRNA half-life using the primers of Fig. 3a. As can be observed in Fig. 3b (lower graph), *MCL1* pA2 mRNA presents the same half-life (approximately 4 h) in resting and activated conditions, consistent with the notion that the increase in pA1 mRNA levels is not due to pA2 mRNA instability upon cell activation. Moreover, no statistically significant alteration was detected in pA1 and pA2 mRNAs half-life (upper graph). These results show that both mRNA isoforms have similar half-lives in resting and activated cellular states. We then quantified MCL1 protein levels by western blot in resting and activated PBMCs, that are constituted by ~ 70% of T cells [65] (Fig. 3c and Supplementary Fig. S1e) and Jurkat E6.1 cells (Fig. 3d and Supplementary Fig. S1e). MCL1 protein levels increase around twofold upon cell activation in these two cell populations, showing a correlation between the increase in pA1 mRNA expression and MCL1 protein levels upon T cell activation.

MCL1 pA1 mRNA is more efficiently translated than pA2 mRNA

The initial observation that short 3′ UTRs correlate with an increase in protein levels in T cells [25] was recently challenged [66]. Therefore, to evaluate the contribution of *MCL1* alternative 3′ UTRs in protein expression, the pA1 and pA2 3′ UTRs were subcloned downstream of a luciferase reporter

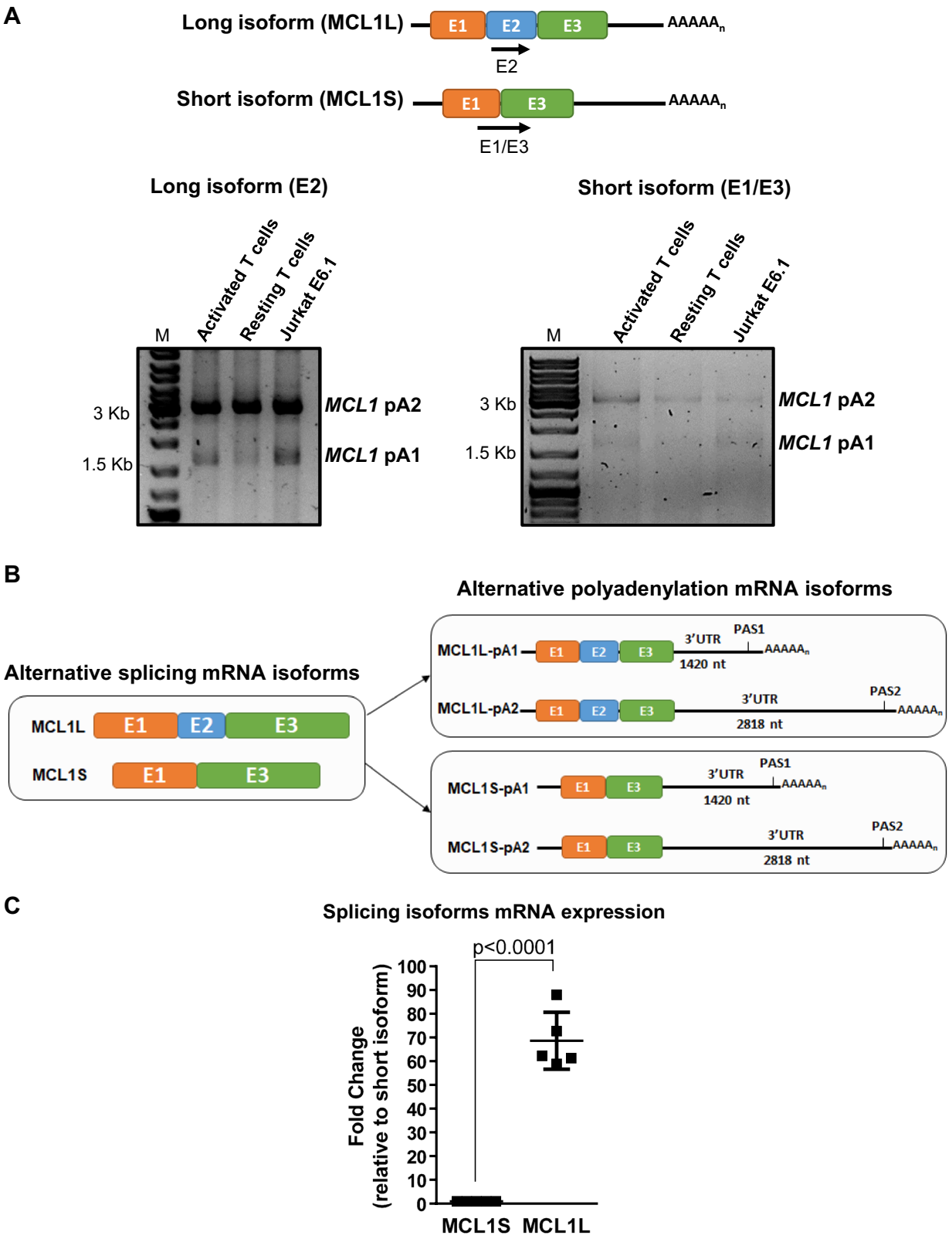
A
Long isoform (MCL1L)
E1
E2
E3
AAAAA$_n$
E2
Short isoform (MCL1S)
E1
E3
AAAAA$_n$
E1/E3
Long isoform (E2)
Short isoform (E1/E3)
M
Activated T cells
Resting T cells
Jurkat E6.1
3 Kb
1.5 Kb
MCL1 pA2
MCL1 pA1
B
Alternative splicing mRNA isoforms
MCL1L
MCL1S
Alternative polyadenylation mRNA isoforms
MCL1L-pA1
MCL1L-pA2
MCL1S-pA1
MCL1S-pA2
3'UTR
PAS1
PAS2
1420 nt
2818 nt
C
Splicing isoforms mRNA expression
p<0.0001
Fold Change (relative to short isoform)
MCL1S
MCL1L

◂**Fig. 2** *MCL1* 3′ UTR alternative polyadenylation is independent from alternative splicing. **A** Schematic illustration of the *MCL1* alternative splicing mRNA isoforms most prevalent in T cells with the position of the primers used in the 3′ RACE. Representative 3′ RACE mapping of the 3′ ends of the *MCL1L* long mRNA isoform (E2) and the *MCL1S* short mRNA isoform (E1/E3) shows that both alternatively spliced mRNA isoforms have the same 3′ ends. A molecular weight DNA ladder is shown on the left. **B** The *MCL1* mRNA isoforms produced in T cells. **C** In primary T cells, the anti-apoptotic long mRNA (*MCL1L*) is 70-fold more expressed than the short pro-apoptotic mRNA (*MCL1S*). Graphic shows the mean ± standard deviation (SD) of five independent experiments using T cells isolated from healthy donors. Unpaired Student t test, ****$p < 0.0001$

gene (Fig. 4a). The luciferase assays show that the short pA1 3′ UTR produces more luciferase activity than the long pA2 3′ UTR (Fig. 4a). Although pA2 mRNA levels are higher (Fig. 4b), the pA1 3′ UTR confers a higher translation efficiency to *Luc* than the pA2 3′ UTR (Fig. 4c). Importantly, this effect is also observed in T cells (Supplementary Fig. S2).

Alternative polyadenylation has a role in gene expression regulation [24] and in protein subcellular localization [4]. MCL1 is mainly localized in the mitochondria [67], therefore, we asked if the different 3′ UTRs affect MCL1 subcellular localization. As can be observed in Fig. 4d, the MCL1 protein expressed from the MCL1-pA1 and MCL1-pA2 constructs (containing EGFP fused to *MCL1* and the short or long 3′ UTR) showed a well-defined mitochondrial distribution, the conventional MCL1 localization [67], and a nuclear staining, which has also been reported [68–70]. Therefore, our results show that the 3′ UTR does not control MCL1 protein subcellular localization. Yet, by confocal microscopy we consistently observed that the MCL1-pA2 construct produce less EGFP than MCL1-pA1 (Fig. 4d), as is clearly shown in the three graphs of Fig. 4e with the quantifications of the fluorescence intensity of MCL1-pA1 and MCL1-pA2 transfected cells. These results were confirmed by western blot (Fig. 4f) and are consistent with the luciferase assay of Fig. 4a. As pA2 mRNA is highly expressed but is less translated, we asked if this isoform was retained in the nucleus. We quantified *MCL1* mRNAs from nuclear and cytoplasmic RNA fractions by performing subcellular RNA fractionation [71] and RT-qPCR with the primer pairs of Fig. 3a. No statistical differences were observed in the cytoplasmic/nuclear ratios between the two conditions indicating that both mRNA isoforms are present and exported to the cytoplasm in the same proportions (Supplementary Fig. S3).

Taken together, our results show that upon T cell activation there is an increase in the levels of the short pA1 mRNA that is translated with higher efficiency than the long pA2 mRNA, leading to an increase in MCL1 protein levels.

MCL1 pA2 mRNA isoform is downregulated by miR-17

To investigate the hypothesis that *MCL1* pA2 mRNA is translationally repressed by miRNAs, we performed an in silico analysis to identify miRNAs that could target the 3′ UTR of *MCL1*. We found > 20 miRNAs predicted to target *MCL1*. Therefore, we applied the following criteria to select the best miRNAs to study: (i) the miRNA must be identified in at least two miRNA databases (TargetScan, microRNA.org, miRbase and miRTarBase), (ii) the miRNA target sequence must be conserved in mammals, and (iii) the miRNA must be expressed in T cells. Four miRNAs were identified fulfilling these criteria: miR-92a, miR-29b, miR-320a and miR-17 (Fig. 5a). We first quantified the expression levels of these four miRNAs in human primary T cells (Fig. 5b). As expected, all miRNAs were expressed in primary T cells. However, only miR-17 and miR-320a expression showed a significant increase of ~ twofold upon T cell activation (Fig. 5b). Of note, these two miRNAs are predicted to target the *MCL1* pA2 mRNA isoform only. Thus, we used luciferase assays to investigate if the miRNAs targeted their respective predicted binding sites on the *MCL1* 3′ UTR. The reporter plasmids contained the miRNA target site (wild type) or the target site mutated by site-directed mutagenesis (Fig. 5c). Mutations in miR-17 and miR-29b target sites led to an increase in luciferase activity but no differences were observed when the putative-target sites of miR-320a and miR-92a were mutated (Fig. 5c). These results indicate that miR-29b and miR-17 modulate *MCL1* expression. We then focused on miR-17 as a possible regulator of *MCL1* pA2 mRNA expression considering that the miR-17–92 cluster is known to modulate T cell fate and function [72], the miR-17 binding site on *MCL1* 3′ UTR is 100% conserved in ten mammalian species (Fig. 5d), and that miR-29b levels do not change upon T cell activation (Fig. 5b).

Accordingly, overexpression of miR-17 downregulates endogenous MCL1 protein expression in both Jurkat E6.1 and HeLa cells (Fig. 5e). We then transfected Jurkat E6.1 and NIH3T3 cells with a luciferase plasmid (Luc-pA2 WT) and a miR-17 mimic or a miRNA negative control (miR-NC) (Fig. 5f). In the presence of miR-17, luciferase activity significantly decreased in comparison to the control in both Jurkat E6.1 and NIH3T3 cell lines. This decrease is relieved by point mutations in the miR-17 target site in Luc-pA2 (Luc-pA2 Mut; black and grey versus yellow bars; Fig. 5f). As expected, no diminution of luciferase activity was observed when the miR-17 binding site is mutated (Luc-pA2 Mut) and co-transfected with miR-17 (Fig. 5f). These results strongly support a model in which *MCL1* pA2 mRNA isoform is post-transcriptionally downregulated by the binding of

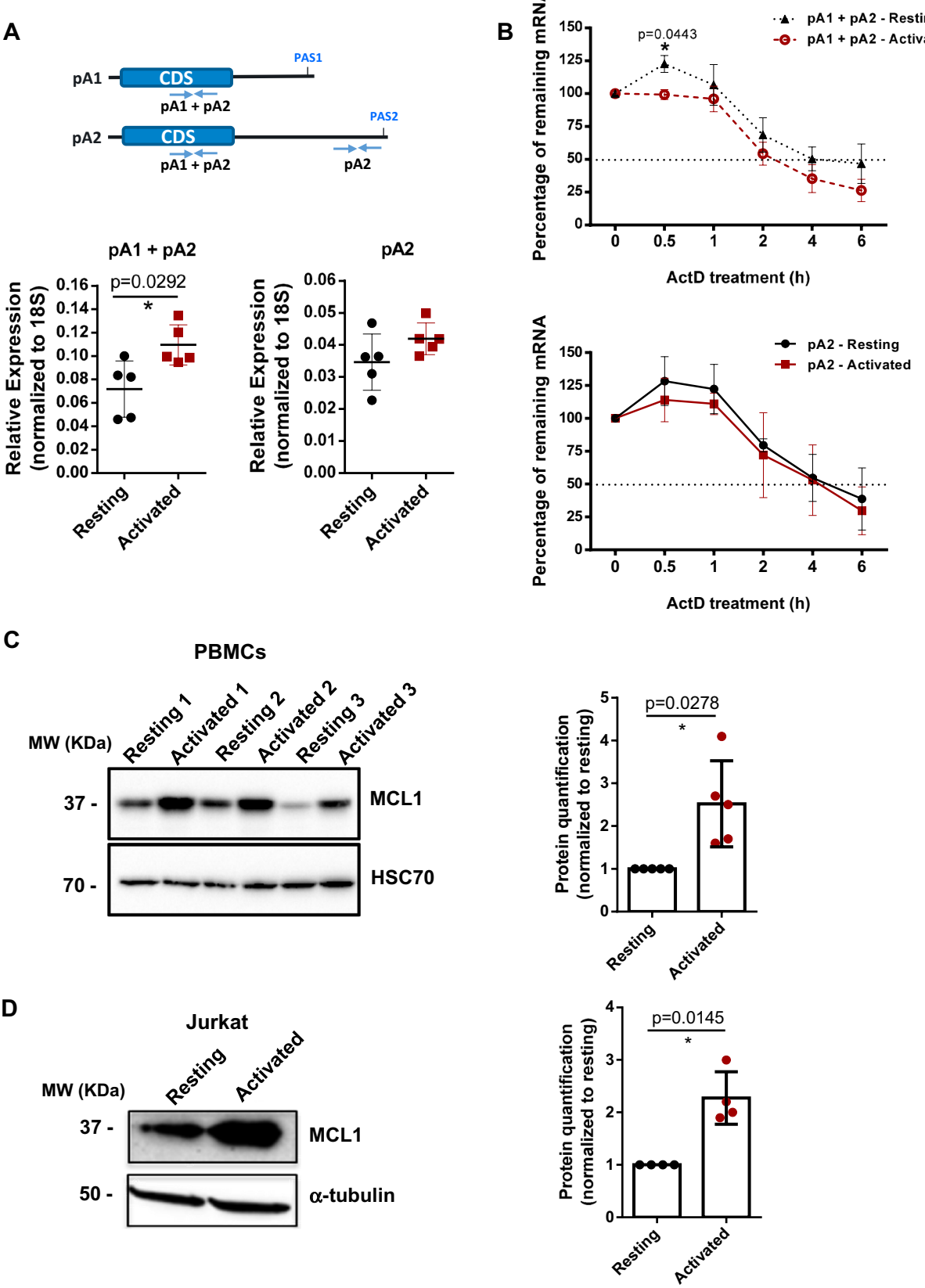
A
pA1
CDS
PAS1
pA1 + pA2
pA2
CDS
PAS2
pA1 + pA2
pA2
pA1 + pA2
pA2
Relative Expression (normalized to 18S)
p=0.0292
*
Resting
Activated
B
pA1 + pA2 - Resting
pA1 + pA2 - Activated
p=0.0443
*
Percentage of remaining mRNA
ActD treatment (h)
pA2 - Resting
pA2 - Activated
C
PBMCs
MW (KDa)
Resting 1
Activated 1
Resting 2
Activated 2
Resting 3
Activated 3
37 -
MCL1
70 -
HSC70
Protein quantification (normalized to resting)
p=0.0278
*
D
Jurkat
MW (KDa)
Resting
Activated
37 -
MCL1
50 -
α-tubulin
p=0.0145
*

◂**Fig. 3** *MCL1* pA1 mRNA expression and protein levels increase upon T cell activation **A** RT-qPCR shows an increase in pA1 mRNA isoform expression upon T cell activation. Primer pair localization are indicated in the scheme, pA1 + pA2 primer pair hybridizes in the coding sequence (CDS) and amplifies both pA1 and pA2 mRNA isoforms. The pA2 primer pair only amplifies the pA2 mRNA isoform. Data show the mean ± standard deviation (SD) of the relative expression normalized to *18S* of five independent experiments using T cells isolated from healthy donors and was analyzed by a two-sided paired *t* test. Significant *p* value (*$p < 0.05$) is indicated in the graph. **B** *MCL1* pA1 and pA2 mRNAs are equally stable in resting and activated T cells. Cells were treated with 5 µg/mL of Actinomycin D for different periods of time, followed by RT-qPCR using *GAPDH* as normalizing control. Graphic shows the mean ± standard deviation (SD) of three independent experiments analyzed by two-way ANOVA with Sidak correction. Significant *p* value (*$p < 0.05$) is indicated in the graph. **C** Representative western blots of MCL1 protein expression in PBMCs isolated from three healthy blood donors and in Jurkat T cells (**D**) show an increase in MCL1 protein levels upon cell activation. HSC70 and α-tubulin were used as loading controls in PBMCs and Jurkat cells, respectively. The quantification of protein levels normalized to the loading control and relative to resting is indicated at the right of each immunoblot ($n = 5$ for PBMCs and $n = 4$ for Jurkat cells, the remaining western blots used for the quantifications can be found in Supplementary Fig S1e) and was analyzed by an Unpaired Student *t* test with Welch's correction. Significant *p* values (*$p < 0.05$) are indicated in the graphs

miR-17 to its target sequence on the longer *MCL1* 3′ UTR. As the binding of miR-17 to the 3′ UTR of the *MCL1* pA2 mRNA is not 100% complementary (Fig. 5f; top scheme), it will repress translation of this isoform [73], explaining its lower levels of translation efficiency.

MCL1 alternative polyadenylation is essential for MCL1 anti-apoptotic function and cell proliferation

To investigate the physiological function of *MCL1* alternative polyadenylation, we used CRISPR/Cas9 genome editing and lentiviral infection to create stable Jurkat E6.1 cells lacking either pA1 (ΔpA1) or pA2 (ΔpA2) isoforms (Supplementary Fig. S4a). Single-cell sorting was performed to obtain ΔpA1 and ΔpA2 homozygous cell populations, but the few clones that survived were heterozygous (Supplementary Fig. S4b and S4c). To circumvent this issue, we performed CRISPR/Cas9 genome editing in HeLa and haploid HAP1 cells. Again, only HeLa heterozygous clones survived (Fig. 6a), and the small number of HAP1 homozygous clones obtained only survived for a few days in culture (Supplementary Fig. S5). Of note, ΔpA1 and ΔpA2 CRISPR/Cas9-edited cells show a strong decrease in pA1 and pA2 polyadenylation signals usage, respectively, in comparison with non-edited cells (Fig. 6b). Moreover, cryptic PAS are used, as expected when a polyadenylation signal is altered or deleted [74, 75]. As a result of deletion of PAS1 and PAS2 signals, ΔpA1 and ΔpA2 cells present reduced MCL1 protein levels in both HeLa (Fig. 6c) and Jurkat E6.1 (Supplementary Fig. S4d).

As MCL1 has a well-recognized anti-apoptotic function [41, 42], we then asked if pA1 and pA2 APA isoforms have a role in cell survival. Quantification of apoptosis levels by Annexin V-PI staining clearly show that ΔpA1 and ΔpA2 cells show an increase in apoptosis and a decrease in cell viability in both HeLa (Fig. 6d and e) and Jurkat E6.1 (Supplementary Fig. S4e and S4f) cells. We then asked if we could rescue the decrease in cell viability in ΔpA1 and ΔpA2 cells by overexpressing each one of the two MCL1 3′ UTR-APA isoforms. We transfected ΔpA1 and ΔpA2 CRISPR cells with the EGFP-MCL1-pA1 or the EGFP-MCL1-pA2 constructs, respectively, to induce overexpression of the APA isoforms. In ΔpA1 and ΔpA2 cells, 24 h post-transfection, there is a dramatic increase in cell death and cell phenotype defects. This is most likely due to the fragility of the cells, which present mitochondrial defects (Fig. 7), low viability (Fig. 6d and Supplementary Fig. S4e) and low proliferation (Fig. 6f), and did not resist transfection. Yet, the few ΔpA1 CRISPR cells transfected with the EGFP-MCL1-pA1 construct (GFP^+ cells) that survived, show an increase in the percentage of live cells (16.9–25.5) and a decrease in apoptotic cells (40.29–27.58), in comparison to the non-transfected cell population (GFP^- cells) (Supplementary Fig. S6b). These results show that the MCL1 pA1 isoform rescues the phenotype displayed by ΔpA1 CRISPR cells. ΔpA2 CRISPR cells were all non-viable after transfection with the EGFP-MCL1-pA2 construct (Supplementary Fig. S6c). These results are in line with a more fragility of these cells as pA2 deletion causes a slight increase in cell death than pA1 deletion (Fig. 6d and Supplementary Fig. S4e). HeLa WT cells transfected with the same constructs did not displayed any visible phenotypical alteration after transfection (Supplementary Fig. S6b and S6c), indicating that the cell death observed was not due to a technical issue related to the transfection, but it was due to characteristics inherent to ΔpA1 and ΔpA2 CRISPR cells. Of note, transfected HeLa WT cells with pA1 or pA2 (GFP^+ cells), (Supplementary Fig. S6b and 6c) have a decrease in the apoptotic cells and an increase in live cells when comparing with the non-transfected population (GFP^- cells), showing that the pA1 and pA2 isoform constructs can lead to an increase in cell viability in the WT cells and confirming the role of these APA isoforms in cell viability.

Taken together, these results clearly indicate that correct regulation of *MCL1* expression by *MCL1* alternative polyadenylation is required for MCL1 anti-apoptotic function.

Considering that MCL1 inhibits the ubiquitin-dependent degradation of cyclin dependent kinase 2 (CDK2) [76] and regulates cell cycle entry [77] and also that ΔpA1 and ΔpA2 CRISPR cells took longer to grow in culture than wild-type or CRISPR-negative control cells, we assessed the role of

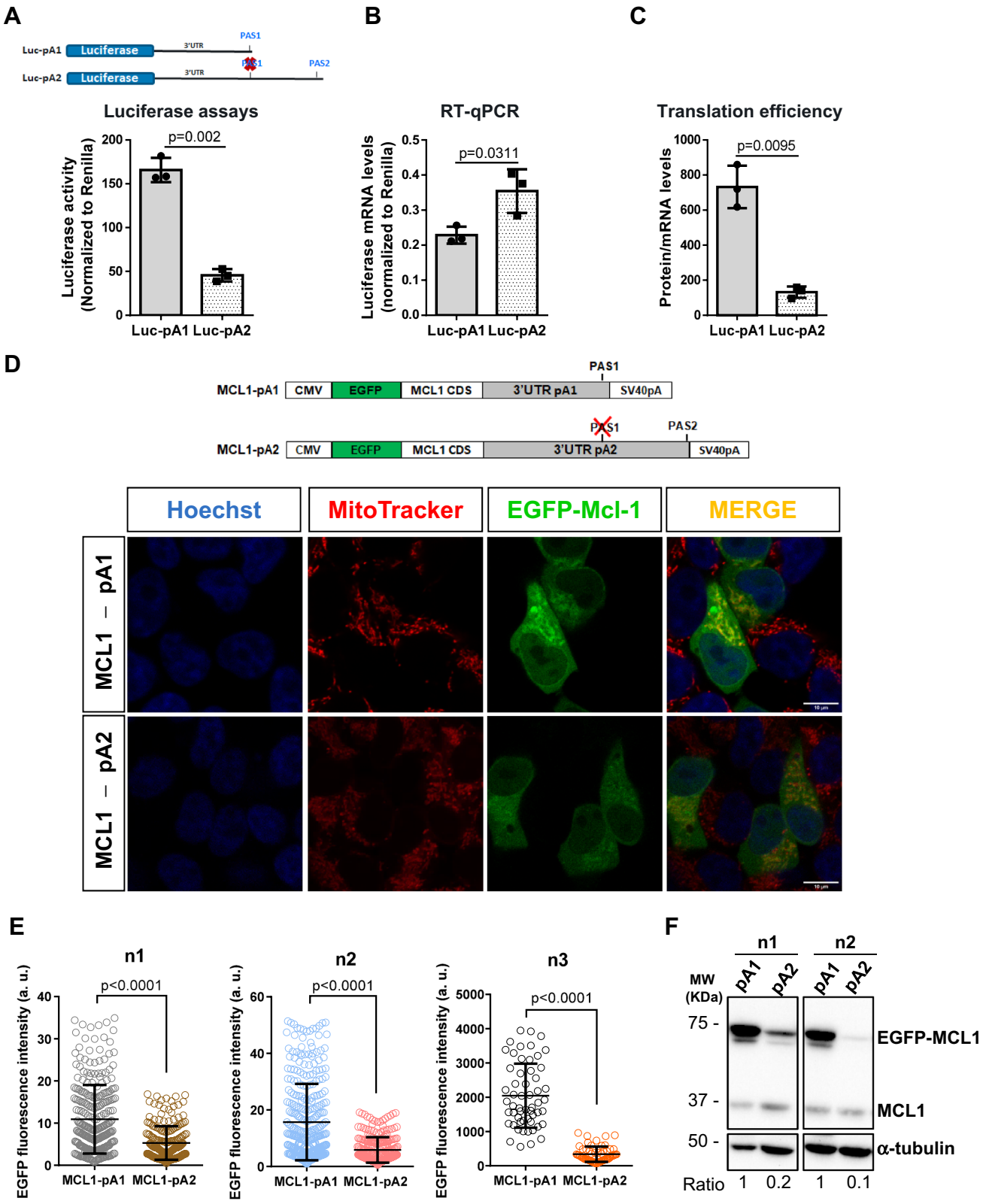
A
Luc-pA1
Luciferase
3'UTR
PAS1
Luc-pA2
Luciferase
3'UTR
PAS1
PAS2
B
C
Luciferase assays
Luciferase activity (Normalized to Renilla)
p=0.002
Luc-pA1 Luc-pA2
RT-qPCR
Luciferase mRNA levels (normalized to Renilla)
p=0.0311
Luc-pA1 Luc-pA2
Translation efficiency
Protein/mRNA levels
p=0.0095
Luc-pA1 Luc-pA2
D
MCL1-pA1
CMV
EGFP
MCL1 CDS
3'UTR pA1
SV40pA
PAS1
MCL1-pA2
CMV
EGFP
MCL1 CDS
3'UTR pA2
SV40pA
PAS1
PAS2
Hoechst
MitoTracker
EGFP-Mcl-1
MERGE
MCL1 – pA1
MCL1 – pA2
E
n1
p<0.0001
EGFP fluorescence intensity (a. u.)
MCL1-pA1 MCL1-pA2
n2
p<0.0001
EGFP fluorescence intensity (a. u.)
MCL1-pA1 MCL1-pA2
n3
p<0.0001
EGFP fluorescence intensity (a. u.)
MCL1-pA1 MCL1-pA2
F
n1
n2
MW (KDa)
pA1
pA2
pA1
pA2
75 -
37 -
50 -
EGFP-MCL1
MCL1
α-tubulin
Ratio 1 0.2 1 0.1

◂**Fig. 4** *MCL1* pA1 mRNA isoform produces more protein than pA2 mRNA isoform because it is more efficiently translated. **A** Top—scheme of the Luciferase reporter constructs containing the two *MCL1* 3′ UTRs subcloned downstream of *Luciferase*. In Luc-pA2, pA1 was mutated. Bottom—graph show that the shortest *MCL1* 3′ UTR (Luc-pA1) confers a higher production of Luciferase activity than the longer *MCL1* 3′ UTR (Luc-pA2). Data show the mean ± standard deviation (SD) of three independent experiments analyzed by Unpaired Student *t* test. Significant *p* value ($p < 0.05$) is indicated in the graph. **B** Luc-pA1 produces lower *Luciferase* mRNA levels that Luc-pA2, assessed by RT-qPCR and normalized to *Renilla* mRNA levels. Data show the mean ± standard deviation (SD) of three independent experiments analyzed by Unpaired Student *t* test. Significant *p* value ($p < 0.05$) is indicated in the graph. **C** Translation efficiency of Luc-pA1 and Luc-pA2 calculated as protein/mRNA ratio shows that Luc-pA1 is more efficiently translated that Luc-pA2 isoform. Data show the mean ± standard deviation (SD) of three independent experiments analyzed by Unpaired Student *t* test. Significant *p* value ($p < 0.05$) is indicated in the graph. **D** Representative fluorescence confocal microscopy images of three independent experiments showing that MCL1-pA1 and MCL1-pA2 display a nuclear and mitochondrial subcellular localization (green). In the MCL1-pA2 construct PAS1 is mutated (schemes of the constructs used are placed above the images). Nuclei are visualized with Hoechst (blue) and mitochondria are labeled with MitoTracker Red (red). Image acquisition was performed using Leica SP5 confocal microscope using the same microscopy settings (laser intensity, zoom, signal gain) and analyzed in ImageJ software. Scale bar is indicated in the lower right side of the merge images (10 µm). **E** Quantification of the EGFP fluorescence intensity obtained by MCL1-pA1 and MCL1-pA2 constructs shows that the longer *MCL1* 3′ UTR (MCL1-pA2) confers a lower MCL1 protein expression than the shorter *MCL1* 3′UTR (MCL1-pA1). Quantification was performed in at least 200 cells in n1 and n2 using a workflow developed specifically for the 2D intensity measurements (see "Materials and methods") and in 50 cells in n3 using Image J and the ROI Manager tool. Images were taken maintaining the same microscopy settings in each independent experience. Outliers were removed in GraphPad using the ROUT method with a Q = 1% of the identify outliers option. Statistical significance was determined by Unpaired Student *t* test with welsh correction. Significant *p* value is indicated in the graphs. **F** EGFP-MCL1-pA1 produces more protein than EGFP-MCL1-pA2, quantified by western blot. MCL1 endogenous protein levels are unaltered as expected. A α-tubulin antibody was used as loading control. The ratio normalized to the loading control and relative to pA1 is shown below the image for the two independent experiments

MCL1 alternative polyadenylation in cell proliferation. We first counted the cells at day 0 and plated the same number of cells in all conditions and counted the cells when the HeLa Wt cells reached 90–95% confluency. The graph of Supplementary Fig. S7 clearly shows that ΔpA1 and ΔpA2 cells have ~ 50% lower division rate than the CRISPR control cells. To validate this observation, we used the cellular dye dilution marker CellTrace Violet (CTV) to perform a cell proliferation assay. We used cells stained with CTV a few hours before the assay (CTV positive) to define the non-proliferative and proliferative populations (Fig. 6f). The histograms and table with the mean fluorescence intensity (gMFI) values in Fig. 6f clearly show that ΔpA1 and ΔpA2 CRISPR cells divide less than the CRISPR control cells, but they are still able to proliferate, as indicated by the lower gMFI value than that of the CTV positive control.

To understand the reason of the poor cell division presented by ΔpA1 and ΔpA2 cells, and as MCL1 is involved in cell division regulation [77] through interactions with cell cycle regulators [78], we performed a cell cycle analysis (Fig. 6g). We observe that there is an increase in ΔpA1 and ΔpA2 cells in G0/G1 phases (ΔpA1-54.4% and ΔpA2-66.8% in comparison to CRISPR control—46.3%), indicative of a G1-arrest, and a there is a decrease in cells in the S-phase (ΔpA1-22.4% and ΔpA2-17.6% in comparison to CRISPR control—32.5%).

The proliferation assay and cell cycle profiles show that ΔpA1 and ΔpA2 CRISPR cells present a decrease in cell proliferation and an alteration in cell cycle progression due to a G1-arrest, sustaining a function for *MCL1* alternative polyadenylation in cell division and proliferation.

MCL1 alternative polyadenylation has a crucial function in mitochondria morphology dynamics

MCL1 was previously described as a mitochondrial morphology regulator [79–82]. Therefore, we assessed if *MCL1* APA mRNAs contribute to this mechanism using the MitoTracker Red CMXRos red-fluorescent dye to stain mitochondria in ΔpA1 and ΔpA2 live cells. Strikingly, ΔpA1 and ΔpA2 cells show clear differences in mitochondria morphology and distribution in comparison to the CRISPR control (Fig. 7a) and WT (Supplementary Fig. S8a) cells. These results indicate that *MCL1* alternative polyadenylation is required for mitochondrial morphology. To better understand this effect, we performed an accurate morphology analysis, by high-throughput image quantification of mitochondria subtypes divided in networks (elongated mitochondria with agglomerations), rods (elongated but small) and puncta (small and round mitochondria) as performed in [83]. The mitochondria segmentation and classification workflow is depicted in Supplementary Fig. S8b. Our results show a significant reduction in the average number of rods and puncta (Fig. 7b and Supplementary Fig. S8c), and a significant increase in the mitochondrial distribution inside the cell (measured as mean distance to nucleus) of the three mitochondrial subtypes in comparison to control cells (Fig. 7c and Supplementary Fig. S8d). These results clearly show that *MCL1* 3′ UTR-APA isoforms impact mitochondria morphology and distribution within the cells. One indication of mitochondrial functional damage is mitochondria swelling [83], therefore, we quantified the mitochondria area. We observed a ~ twofold increase in the area of networks, as well as a significant increase in rods area, in comparison to control cells (Fig. 7d and Supplementary Fig. S8e). In ΔpA2, we observed a reduction in the puncta area when comparing with CRISPR control (Fig. 7d). These results

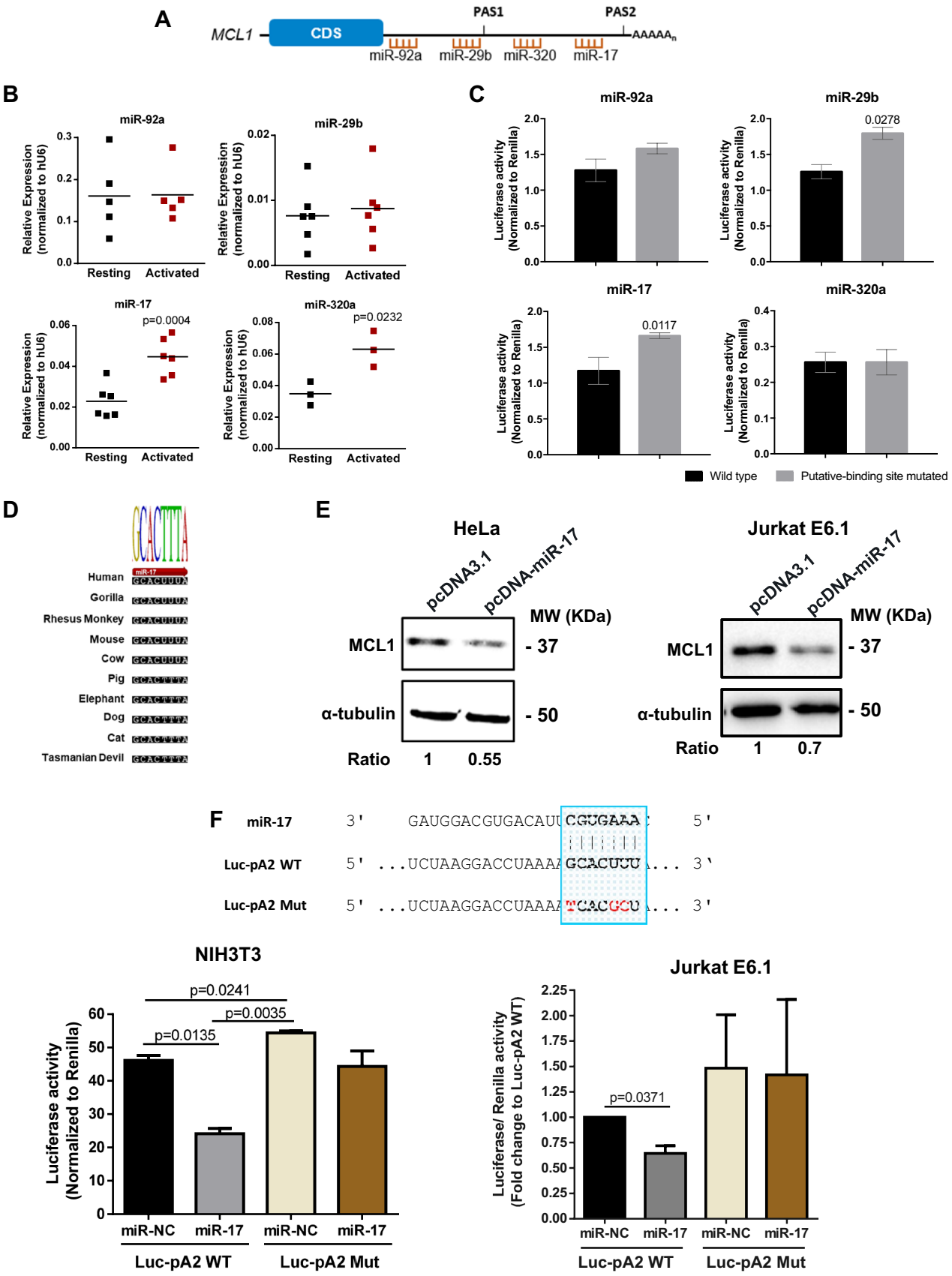
A
MCL1
CDS
PAS1
PAS2
AAAAA$_n$
miR-92a
miR-29b
miR-320
miR-17
B
miR-92a
miR-29b
miR-17
miR-320a
Relative Expression (normalized to hU6)
Resting
Activated
p=0.0004
p=0.0232
C
miR-92a
miR-29b
miR-17
miR-320a
Luciferase activity (Normalized to Renilla)
0.0278
0.0117
Wild type
Putative-binding site mutated
D
Human
Gorilla
Rhesus Monkey
Mouse
Cow
Pig
Elephant
Dog
Cat
Tasmanian Devil
E
HeLa
Jurkat E6.1
pcDNA3.1
pcDNA-miR-17
MW (KDa)
MCL1
α-tubulin
- 37
- 50
Ratio
1
0.55
0.7
F
miR-17
Luc-pA2 WT
Luc-pA2 Mut
3'
5'
NIH3T3
Jurkat E6.1
Luciferase activity (Normalized to Renilla)
Luciferase/ Renilla activity (Fold change to Luc-pA2 WT)
p=0.0241
p=0.0035
p=0.0135
p=0.0371
miR-NC
miR-17
Luc-pA2 WT
Luc-pA2 Mut

◂**Fig. 5** miR-17 is upregulated upon T cell activation and downregulates *MCL1* pA2 mRNA isoform. **A** Scheme depicting the location of the four selected miRNAs (miR-92a, miR-29b, miR-320a and miR-17) putative-binding sites on *MCL1* 3′ UTR. **B** miR-17 and miR-320a significantly increase their expression upon T cell activation. miRNAs' relative expression was quantified by RT-qPCR in resting and activated primary T cells from three healthy donors for miR-320a, five healthy donors for miR-92a and six healthy donors for miR-17 and miR-29b, and analyzed using a paired Student *t* test. Significant *p* values ($p < 0.05$) are indicated in the respective graph. *U6* was used as a normalizing control. (**C**) Only mutations in miR-17 and miR-29b binding sites led to an increase in luciferase activity. Luciferase reporter plasmids with the miRNAs binding site (black bars; Wild type) or with the mutated binding site (grey bars) were transfected in NIH3T3 cells. Data show the mean ± standard deviation (SD) of three independent experiments analyzed by unpaired Student *t* test. Significant *p* values ($p < 0.05$) are indicated in the respective graph. **D** The putative miR-17 target site in the 3′ UTR of *MCL1* is 100% conserved across ten mammalian species, including the marsupial Tasmanian devil. The sequence logo is represented above the multiple sequence alignment. **E** miR-17 overexpression (pcDNA-miR-17 transfected cells) downregulates endogenous MCL1 protein in HeLa and Jurkat E6.1 cells. Western blot was performed for MCL1 protein and α-tubulin was used as a loading control. MCL1 quantification normalized to loading control and relative to the pcDNA3.1 empty vector is indicated below the immunoblot. **F** miR-17 targets *MCL1* pA2 mRNA isoform. The miR-17 sequence, its target site on *MCL1* 3′ UTR and mutated binding site are highlighted by a blue box. Luciferase reporter plasmids with the miR-17 binding site (WT) or with the mutated binding site (Mut), a negative control (miR-NC) or a miR-17 mimics (miR-17), were transfected in NIH3T3 (left graph) and Jurkat E6.1 cells (right graph). Luciferase activity shows that in both cell lines, miR-17 downregulates luciferase activity of the wild-type pA2 (Luc-pA2 WT) construct but not of the construct with miR-17 binding site mutation (Luc-pA2 Mut). Data show the mean ± standard deviation (SD) of three independent experiments analyzed by one-way ANOVA. Significant *p* values ($p < 0.05$) are indicated in the graph

show that both MCL1 APA mRNA isoforms contribute to mitochondria morphology and dynamics.

We then asked if ΔpA1 and ΔpA2 cells present alterations in proteins involved in mitochondrial dynamics by analyzing DRP1, MFN1 and MFN2 in ΔpA1 and ΔpA2 cells. As it can be observed in the western blots in Fig. 7e, both ΔpA1 and ΔpA2 CRISPR cells show a decrease in DRP1 levels in comparison to the controls. MCL1 interacts with DRP1 to promote mitochondrial fission in a DRP1-dependent manner [79]. Our results are in agreement with a decrease in MCL1 and DRP1 protein levels in ΔpA1 and ΔpA2 CRISPR cells that lead to the morphological changes observed in mitochondria (Fig. 7a), a decrease in rods and puncta (Fig. 7b and Supplementary Fig. S8c) and an increase of the distance to the nucleus (Fig. 7c and Supplementary Fig. S8d), indicating a decrease in mitochondrial fission.

We also observe that deletion of pA1 and pA2 lead to an increase in MFN1 and MFN2 levels (Fig. 7e). As these mitofusins are required for mitochondrial fusion [84, 85], these results are also consistent with the changes in mitochondrial morphology observed in ΔpA1 and ΔpA2 CRISPR cells: an increase in mitochondria area (Fig. 7d and Supplementary Fig. S8e), a decrease in rods and puncta (Fig. 7b and Supplementary Fig. S8c) and more elongated mitochondria (Fig. 7a), which are more distant to the nucleus (Fig. 7c and Supplementary Fig. S8d), all possible indications of an increase in fusion.

These results indicate that alterations in mitochondrial morphology presented by ΔpA1 and ΔpA2 cells involve changes in mitochondrial dynamics proteins. As mitochondria have a fundamental role in providing most of the ATP necessary for biochemical and cellular functions, these results explain the essential function of *MCL1* APA in cell viability.

Discussion

Genome-wide studies revealed that APA is a regulatory mechanism relevant for the immune system and in T cells [23, 25, 27, 66]. Yet, how this mechanism impacts on the expression of single genes and its physiological relevance remains mostly unknown. Here we focus on *MCL1*, a gene with an important anti-apoptotic function in the immune system, which is essential for T cell development, maintenance and survival [38, 42]. In human primary T cells, *MCL1* produces two splicing mRNA isoforms with opposite functions. The canonical long variant (*MCL1L*) is the most expressed form and is anti-apoptotic, whereas the short mRNA isoform (*MCL1S*) is pro-apoptotic [63, 64]. Previous studies focused on the regulation of *MCL1* by alternative splicing, but the function of APA in *MCL1* regulation was unexplored.

We started by mapping *MCL1* 3′ ends by 3′ RACE and found two mRNA isoforms, that we named pA1 and pA2, generated by the usage of two canonical polyadenylation signals (PAS) in the 3′ UTR (3′ UTR-APA). *MCL1* pA1 and pA2 mRNA isoforms share the same coding sequence but vary in the length of their 3′ UTRs. Although weaker PAS variants are usually present in proximal PAS [11], *MCL1* has two strong canonical PAS, which prompted us to investigate the physiological functions of *MCL1* alternative 3′ UTRs and *MCL1* 3′ UTR-APA regulation. We found that *MCL1* alternative polyadenylation is independent of alternative splicing as both *MCL1L* and *MCL1S* mRNAs have the same 3′ ends. Both splicing isoforms use the two canonical PAS present in the 3′ UTR originating pA1 and pA2 mRNA isoforms. As *MCL1S* is little expressed in T cells (70-fold less) we focused on studding *MCL1L* APA isoforms.

The 3′ UTR is a hub for gene expression regulation as it harbors important *cis*-regulatory motifs [24, 86]. *MCL1* 3′ UTR is 65.5% conserved in ten mammals, including the marsupial Tasmanian devil. This level of conservation is particularly high for a 2818-nucleotide 3′ UTR, as non-coding sequences are prone to accumulate mutations

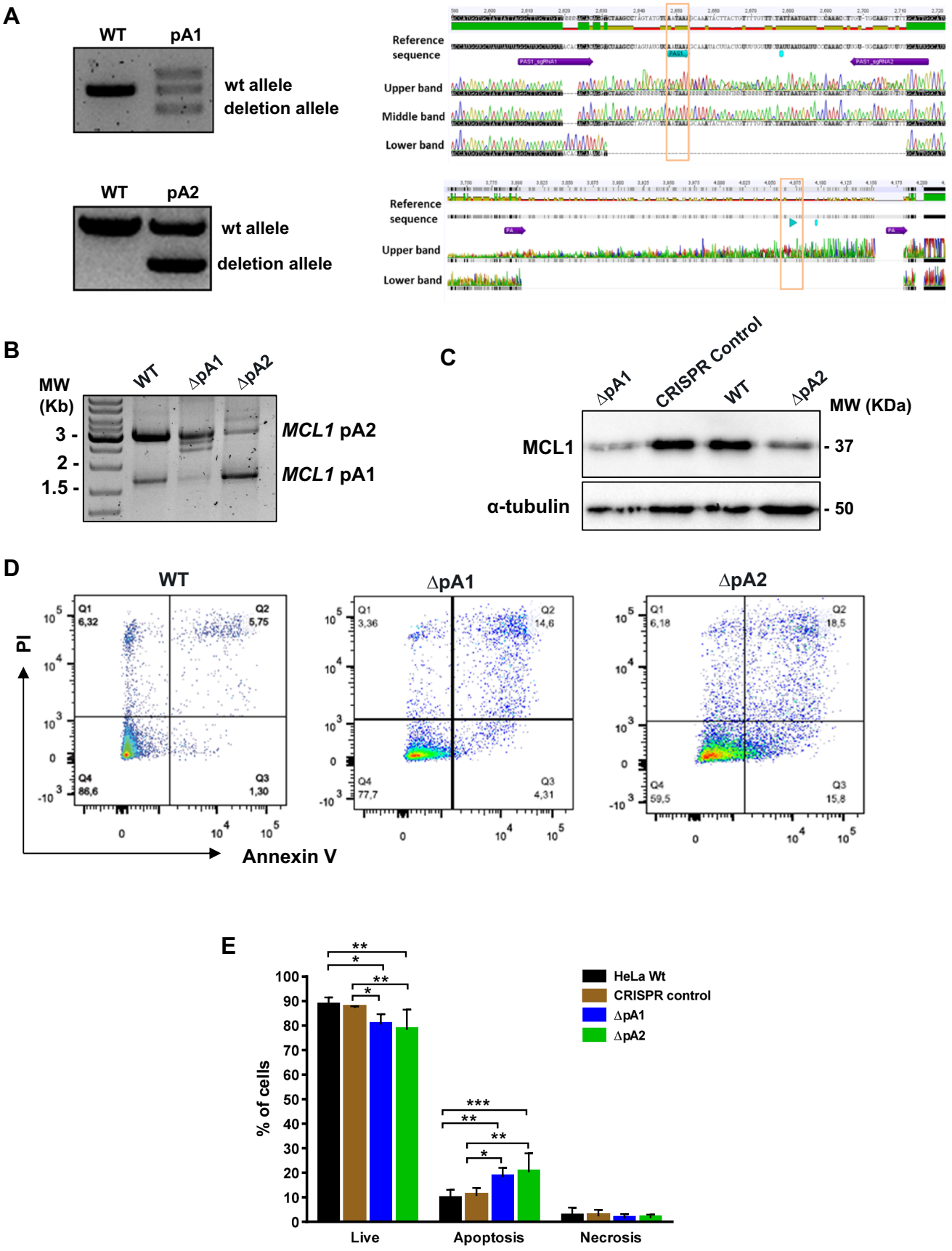
A
WT
pA1
wt allele
deletion allele
Reference sequence
Upper band
Middle band
Lower band
WT
pA2
wt allele
deletion allele
Reference sequence
Upper band
Lower band
B
MW (Kb)
WT
ΔpA1
ΔpA2
3 -
2 -
1.5 -
MCL1 pA2
MCL1 pA1
C
ΔpA1
CRISPR Control
WT
ΔpA2
MW (KDa)
MCL1
- 37
α-tubulin
- 50
D
WT
ΔpA1
ΔpA2
PI
Annexin V
Q1 6,32
Q2 5,75
Q4 86,6
Q3 1,30
Q1 3,36
Q2 14,6
Q4 77,7
Q3 4,31
Q1 6,18
Q2 18,5
Q4 59,5
Q3 15,8
E
% of cells
HeLa Wt
CRISPR control
ΔpA1
ΔpA2
Live
Apoptosis
Necrosis

◂**Fig. 6** *MCL1* pA1 and pA2 mRNA APA isoforms contribute to MCL1 anti-apoptotic function and cell proliferation. **A** Genotyping of CRISPR/Cas9-edited HeLa cells. On the left, PCRs showing ΔpA1 or ΔpA2 genotyping in comparison with non-edited cells (WT). Amplicon sizes are indicated on the left of the gels. On the right, sequencing results obtained by DNA purification of all the ΔpA1 and ΔpA2 bands. The electropherograms show that genome editing was done successfully in heterozygosity. Blue arrows and orange box correspond to the PASs, blue boxes to the polyA sites and purple arrows to the sgRNAs. **B** Representative 3′ RACE image shows that the deletion of the PAS1 in ΔpA1 and PAS2 in ΔpA2 cells occurred successfully, resulting in the utilization of polyadenylation signals PAS2 and PAS1, respectively. **C** Heterozygous ΔpA1 and ΔpA2 CRISPR/Cas9-edited cells display a reduction of MCL1 protein levels in comparison with WT cells and a CRISPR-negative control. Western blot was performed using a MCL1 antibody and α-tubulin as a loading control. **D** and **E** Depletion of pA1 or pA2 in HeLa cells causes a decrease of live cells and an increase in the apoptosis levels, indicating that both APA mRNA isoforms contribute to MCL1 anti-apoptotic function. **D** Representative dot plots of Annexin V-PI staining followed by Flow Cytometry analysis performed in WT, ΔpA1 and ΔpA2 heterozygous cells. Q1 (necrosis); Q2 (late apoptosis); Q3 (early apoptosis); Q4 (live cells). Data in the graph **F** show the mean ± standard deviation (SD) of three independent Annexin V-PI experiments analyzed by two-way ANOVA with Turkey correction. Significant *p* values indicated by asterisks are: $*p<0.05$, $**p<0.01$ and $***p<0.001$. The exact *p* values can be found in Supplementary Table S3. In the graph, early and late apoptosis values were combined and represented as apoptosis. **F** Deletion of either pA1 or pA2 cause a decrease in cell proliferation. Gating strategy is shown in the left. Histogram plots show proliferating cells relative to non-dividing proliferating control (CTV positive cells). ΔpA1 and ΔpA2 cells have higher Geometric mean (gMFI) values that the CRISPR control, shown in the table. Cell proliferation assays were performed by CellTrace Violet (CTV) staining followed by Flow Cytometry analysis in CRISPR-negative control, ΔpA1- and ΔpA2-edited cells. **G** ΔpA1 and ΔpA2 cells have alterations in the cell cycle phase distribution. Representative histograms of the cell cycle profiles after Propidium iodide staining (blue: G0/G1, Brown: S; green: G2/M). ΔpA1 and ΔpA2 cells show a G0/G1-arrest and a decrease in the S-phase in comparison with the CRISPR control cells. Cell cycle phases' percentages are shown in each histogram. Data were analyzed using the Dean-Jett Fox (DJF) model and all histograms have a Root Mean Square (RMS) error below 4

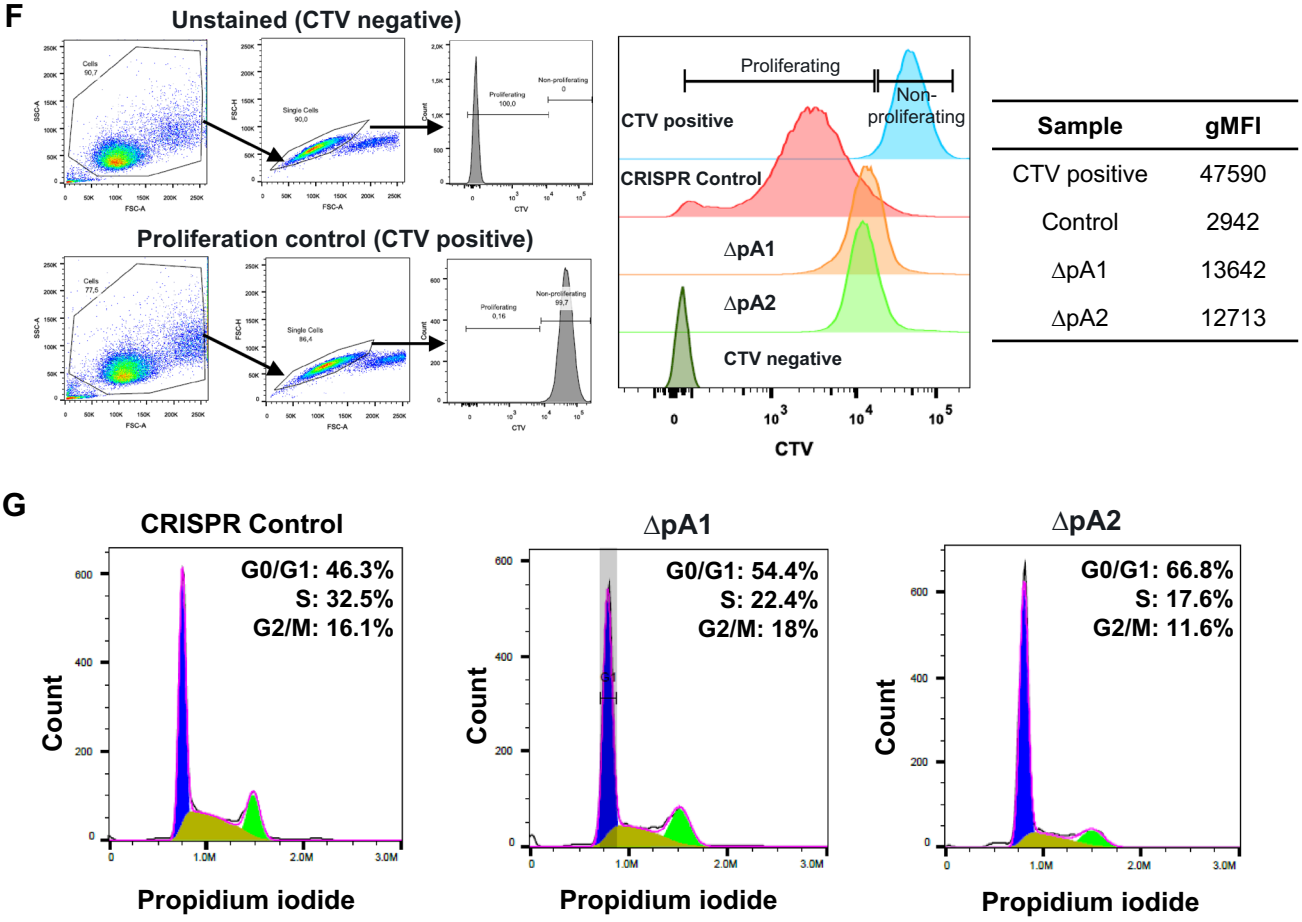

Sample	gMFI
CTV positive	47590
Control	2942
ΔpA1	13642
ΔpA2	12713

Fig. 6 (continued)

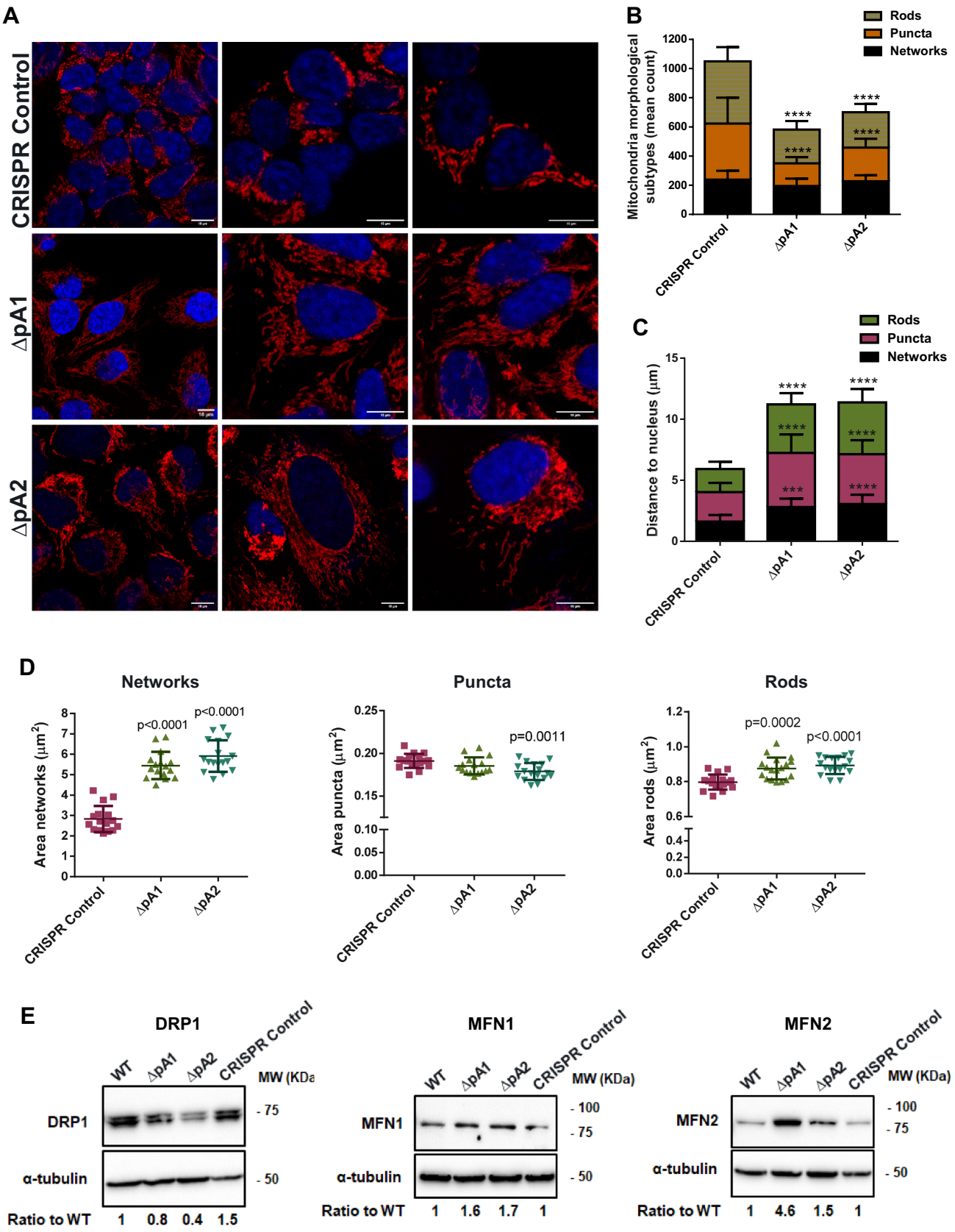
A
CRISPR Control
ΔpA1
ΔpA2
B
Rods
Puncta
Networks
Mitochondria morphological subtypes (mean count)
1200
1000
800
600
400
200
0
****
CRISPR Control
ΔpA1
ΔpA2
C
Rods
Puncta
Networks
Distance to nucleus (μm)
15
10
5
0
****
***
CRISPR Control
ΔpA1
ΔpA2
D
Networks
Area networks (μm²)
p<0.0001
p<0.0001
Puncta
Area puncta (μm²)
p=0.0011
Rods
Area rods (μm²)
p=0.0002
p<0.0001
CRISPR Control
ΔpA1
ΔpA2
E
DRP1
MFN1
MFN2
WT
ΔpA1
ΔpA2
CRISPR Control
MW (KDa)
DRP1
α-tubulin
- 75
- 50
Ratio to WT 1 0.8 0.4 1.5
MFN1
- 100
- 75
- 50
Ratio to WT 1 1.6 1.7 1
MFN2
- 100
- 75
- 50
Ratio to WT 1 4.6 1.5 1

◂**Fig. 7** *MCL1* ΔpA1 and ΔpA2 CRISPR/Cas9-edited cells show defects in mitochondria morphology. **A** Representative live-cell fluorescence confocal microscopy images showing that deletion of pA1 and pA2 affects mitochondria distribution and morphology when compared with the CRISPR-negative control. Nuclei were visualized with Hoechst (blue) and mitochondria were labeled with MitoTracker Red CMXRos (red). Scale bar is indicated at the lower right side of each image. **B** Deletion of pA1 and pA2 reduce the number of puncta and rods mitochondrial subtypes by half, in comparison to the CRISPR control. Graphs show mitochondrial subtypes mean count ± standard deviation (SD) analyzed by 2-way ANOVA with Turkey correction, significant *p* values ($p < 0.0001$) in comparison with the CRISPR control are represented by ****. **C** ΔpA1 and ΔpA2 cells show alterations in mitochondria distribution detected by an increase in the mean distance of the mitochondria structures to the nucleus. Graphs indicate the mean distance of networks, puncta and rods to the nucleus ± standard deviation (SD) analyzed by 2-way ANOVA with Turkey correction and significant *p* values in comparison with the CRISPR control are: ***$p = 0.0007$ and ****$p < 0.0001$. **D** ΔpA1 and ΔpA2 cells show an increase in the area of networks and rods in comparison to the CRISPR control. ΔpA2 cells show a decrease in the area of the puncta. Graphs indicate the quantification of changes in the mean area of each mitochondria morphological subtype (networks, puncta and rods) ± standard deviation (SD) analyzed by one-way ANOVA with Turkey correction. Significant *p* values ($p < 0.05$) in comparison to the CRISPR control are indicated in the graph. **E** ΔpA1 and ΔpA2 CRISPR-edited cells display alteration in the levels of mitochondrial dynamics proteins. Western blots show a reduction of DRP1 protein levels in comparison to the WT cells and to the CRISPR control (left) and an increase of MNF1 (middle) and MNF2 (right) proteins in comparison with WT cells and the CRISPR control. The quantification of protein levels normalized to the α-tubulin loading control and relative to the WT is indicated below each immunoblot

due to the absence of selective constraints [87, 88]. Therefore, the strong selective pressure to maintain *MCL1* 3′ UTR sequences unaltered throughout evolution suggests that this region has a function in *MCL1* gene expression regulation. Notably, *MCL1* orthologues also possess two conserved canonical PAS, suggesting that *MCL1* 3′ UTR-APA is conserved.

Previous genome-wide studies have established a correlation between cell activation and proximal PAS selection [25]. In activated T cells, there is an increase in the expression of mRNAs with shorter 3′ UTRs, which are less susceptible to post-transcriptional regulation [25]. We show that while *MCL1* pA2 mRNA isoform is highly expressed in resting and activated T cells, the levels of the short *MCL1* pA1 mRNA are twofold increased upon activation of human primary T cells, and that this effect is not due to different mRNA stabilities. We also show that MCL1 protein levels increase after T cell activation. This effect is not due to pA2 mRNA instability or nuclear retention, but due to the increase in pA1 mRNA levels and to a higher translation efficiency exhibited by this mRNA isoform, both contributing to the increase in MCL1 protein expression. It is intriguing that *MCL1* pA2 mRNA isoform is highly expressed in resting and activated cells, while it is the *MCL1* pA1 mRNA isoform that mostly contribute for the MCL1 protein levels. We hypothesize that the function of the *MCL1* pA2 mRNA isoform is to provide "basal" levels of MCL1 protein necessary for cell maintenance, independently of the state of the cell. After an external cue, the cells require an additional amount of MCL1 protein that is provided by pA1 mRNA, which was increased and is more efficiently translated. This APA event, together with the different levels of translation efficiency provided by the two 3′ UTRs, assure that the correct MCL1 levels are maintained for cell homeostasis in resting and activated conditions. As *MCL1* is vital for activated T cells [38], 3′ UTR-APA is thus necessary to fine-tune MCL1 expression by providing the cell with the appropriate MCL1 protein levels required for cell survival.

MCL1 is a key factor in T cells maintenance and it is likely that its expression is controlled by multiple mechanisms. miRNAs are known post-transcriptional regulators of 3′ UTR-APA mRNA isoforms [2], as described for *FNDC3B* in nasopharyngeal carcinoma [89], *Pax3* in muscle stem cells [36], and *CD5* in activated T cells [33]. Moreover, mRNAs with short 3′ UTRs can escape miRNA regulation, as described in cancer cells [28], in macrophages after bacterial infection [27], and in activated T cells [25]. We found that miR-17 targets the long *MCL1* pA2 mRNA isoform. It is worth mentioning that miR-17 belongs to the miR-17-92 cluster, which is known to modulate T cell fate and function [72] and is frequently overexpressed in different tumors, including hematological cancers [90]. We found that miR-17 expression increases significantly upon T cell activation, targets *MCL1* pA2 mRNA and downregulates endogenous MCL1 protein. Importantly, miR-17 target site on *MCL1* pA2 3′ UTR is 100% conserved in mammals, indicating a conserved functional role for miR-17 in *MCL1* post-transcriptional regulation. These results indicate that *MCL1* pA2 mRNA expression is regulated by miR-17, and explains why this mRNA isoform is less efficiently translated than *MCL1* pA1 mRNA.

It has been described that CD47 3′ UTR-APA has a function in the localization of CD47 in the plasma membrane [4]. We investigated a possible function of the alternative 3′ UTRs in MCL1 subcellular localization considering that MCL1 localizes in the mitochondrial outer membrane [67, 68, 91], in accordance with its anti-apoptotic function [40, 67], and also in the nucleus in response to DNA damage [69, 70]. However, we did not observe a different subcellular localization for EGFP-MCL1-pA1 and EGFP-MCL1-pA2 proteins. We found that both proteins are localized in the mitochondria, in agreement with its anti-apoptotic function, and in the nucleus, which may be required for the non-apoptotic functions of MCL1 [92].

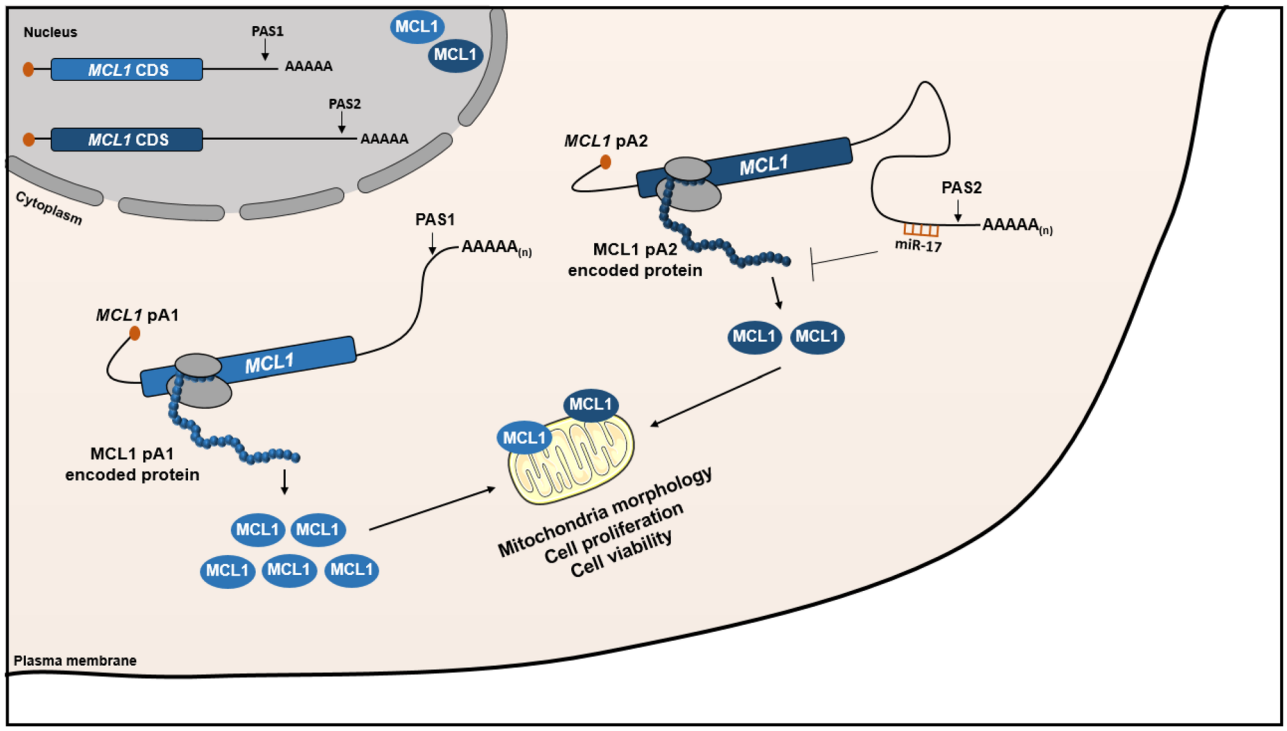

Fig. 8 Proposed model for *MCL1* 3′ UTR-APA regulation and function of the alternative *MCL1* 3′ UTRs. *MCL1* produces two mRNA isoforms (pA1 and pA2) by 3′ UTR alternative polyadenylation. Upon cell activation, there is an increase in the expression of the short pA1 mRNA isoform that is more efficiently translated originating more MCL1 protein. miR-17 contributes to the regulation of *MCL1* pA2 mRNA levels during T cell activation, helping fine tuning MCL1 protein levels. Both *MCL1* 3′ UTR-APA mRNA isoforms are essential for MCL1 function in cell viability and proliferation, and for mitochondria morphology

It is well established that alternative 3′ UTRs influence mRNA stability, localization and translation [5–7], but surprisingly, little is known about the biological relevance of the 3′ UTR-APA. Although animal models have been used to investigate 3′ UTR-APA physiological function as previously shown for *polo* in *Drosophila* [35], vertebrate models where *MCL1* is expressed are difficult to produce, time-consuming and physiological effects are often difficult to distinguish. To circumvent this limitation, we deleted *MCL1* PAS1 and PAS2 polyadenylation signals in Jurkat E6.1, HAP1 and HeLa cell lines by CRISPR/Cas9. Surprisingly, ΔpA1 or ΔpA2 homozygous cells were lethal, suggesting that both mRNAs are essential, revealing a vital physiological function for *MCL1* 3′ UTR-APA. MCL1 controls cell cycle progression by engaging Proliferating Cell Nuclear Antigen (PCNA), Cyclin-dependent kinase 1 (Cdk1) [69] and Cdk2 [76]. Notably, in heterozygosity, we observed that ΔpA1 or ΔpA2 affects the anti-apoptotic function of MCL1, cell proliferation and cell cycle progression, sustaining an essential role for alternative polyadenylation in *MCL1* physiological functions.

Mitochondria are dynamic organelles that change their morphology and activity in response to physiological changes and pathological conditions. These morphological alterations affect the mitochondria function in key cellular processes, including oxidative phosphorylation and programmed cell death [80, 93]. Previous studies have described a role for MCL1 in mitochondrial dynamics regulation [67, 79–82]. Loss of Mcl-1 in mouse myocytes leads to mitochondrial swelling and remodeling [82], MCL1 was shown to play a role in mitochondrial structure maintenance in stem cells [81] and to regulate normal mitochondrial fission and fusion in mouse embryonic fibroblasts [67]. Mitochondrial dynamics is maintained in healthy cells through a tight balance between mitochondrial fission and fusion processes [93]. As both *MCL1* APA-encoded proteins localize in the mitochondria, we evaluated their function in mitochondrial structure and dynamics. We show that both *MCL1* pA1 and pA2 mRNAs are required for proper mitochondria morphology. Mitochondria of ΔpA1 and ΔpA2 CRISPR-edited cells are larger and more elongated in comparison to control cells, and present dramatic changes in mitochondrial structures. In particular, ΔpA1 and ΔpA2 present a twofold

decrease in the number of puncta and rods and a twofold increase in the mitochondria cellular distribution (measured as mean distance to nucleus). Notably, networks and rods of ΔpA1 and ΔpA2 mitochondria present a significant increase in their mean area, indicating mitochondria swelling and damage [83]. In addition, ΔpA1 and ΔpA2 cells show alterations in the levels of DRP1, MFN1 and MFN2 mitochondrial proteins. DRP1 is involved in mitochondrial fission and MFN1/2 in mitochondrial fusion [80, 84, 94]. ΔpA1 and ΔpA2 cells show a decrease in DRP1 and an increase in MFN1/2 protein levels further sustaining the altered phenotype observed in the mitochondria of these cells and clarifying the mechanisms involved in the mitochondrial morphology alterations observed [84, 94]. As MCL1 [79], mitofusins and DRP1 are also implicated in the regulation of apoptosis [95, 96], our results further indicate an interplay between mitochondria dynamics regulation and apoptosis. As mitochondrial dynamics is determinant of its function, alterations in mitochondria morphology and structure lead to severe cellular imbalances and are most likely responsible for the observed cell death, demonstrating how essential the function of *MCL1* APA is for cell viability.

Taken together, we provide the first detailed characterization of the physiological function of the *MCL1* 3′ UTR-APA in mitochondria dynamics and identified miR-17 as modulators of *MCL1* expression (proposed model in Fig. 8). Our results show that *MCL1* alternative polyadenylation has a key function in providing the appropriate MCL1 protein levels, essential for maintaining a healthy mitochondrial dynamics and fitness during T cell activation, cell proliferation and survival, when high energetic demands are required to maintain cell homeostasis.

Supplementary Information The online version contains supplementary material available at https://doi.org/10.1007/s00018-022-04172-x.

Acknowledgements The authors acknowledge the support of the i3S Scientific Platforms: Advanced Light Microscopy and Bioimaging, members of national infrastructure PPBI (supported by POCI-01-0145-FEDER-022122), Translational Cytometry Scientific Platform and Genomics Platform. The authors would like to thank *Serviço de Imunohemoterapia* of *Centro Hospitalar Universitário de São João (CHUSJ)*, Porto for kindly donating the buffy coats. We are very grateful to Eric J. Wagner (UTMB, Houston, USA) and Joel R. Neilson (Baylor College of Medicine, Houston, USA) for reagents and helpful discussions and Elsa Logarinho, Catarina Meireles, Emília Cardoso and Rita Santos (i3S, Porto, Portugal) for the useful discussions on cytometry data.

Author contributions IP-C designed and performed the experiments, analyzed the data and wrote the manuscript; BCG contributed to the experiments with the CRIPR/Cas9 cell lines; AC contributed to the miRNA experiments; AN-C generated some of the lentivirus used in this work; EC-S analyzed the mitochondria microscopy images and develop the workflows for image analysis; LFM contributed with intellectual input and revised the manuscript; AM designed and supervised the project and wrote the manuscript. All the authors have read and approved the final version of the manuscript.

Funding This work was funded by Fundo Europeu de Desenvolvimento Regional (FEDER) funds through the COMPETE 2020-Operational Program for Competitiveness and Internationalisation (POCI), Portugal 2020, and by Portuguese funds through Fundação para a Ciência e a Tecnologia (FCT)/Ministério da Ciência, Tecnologia e Ensino Superior, in the framework of the project Institute for Research and Innovation in Health Sciences (POCI-01–0145-FEDER-007274). This study was also supported by the "Cancer Research on Therapy Resistance: From Basic Mechanisms to Novel Targets"—NORTE-01–0145-FEDER-000051 project, supported by Norte Portugal Regional Operational Programme (NORTE 2020), under the PORTUGAL 2020 Partnership Agreement, through the European Regional Development Fund (ERDF), by the European Union's Horizon 2020 research and innovation programme under grant agreement No 952334, by FCT under the project EXPL/SAU-PUB/1073/2021 and by Programa Operacional Regional do Norte and co-funded by European Regional Development Fund under the project "The Porto Comprehensive Cancer Center" with the reference NORTE-01–0145-FEDER-072678—Consórcio PORTO.CCC—Porto Comprehensive Cancer Center. EC-S was supported by the project PPBI-POCI-01–0145-FEDER-022122 in the scope of Fundação para a Ciência e Tecnologia, National Roadmap of Research Infrastructures. IP-C is funded by a Junior Researcher contract (DL 57/2016/CP1355/CT0016).

Availability of data and material The workflow for mitochondrial morphology analysis as well as the training datasets used can be downloaded from: https://github.com/econdesousa/ImageAnalysis/tree/master/MitochondrialStats and the workflow for the cell segmentation performed for the 2D intensity measurements can be downloaded from: https://github.com/econdesousa/CellPoseSegPlusIntensityMeasurement. Additional data that support the findings of this work are available upon request.

Declarations

Conflict of interest The authors declare that there is no conflict of interest.

Ethics approval and consent to participate The isolation of immune cells from buffy coats of healthy blood donors was approved by the Centro Hospitalar Universitário São João Ethics Committee (protocol 90/19), after each donor informed consent collection.

Consent for publication Not applicable.

References

1. Derti A et al (2012) A quantitative atlas of polyadenylation in five mammals. Genome Res 22(6):1173–1183
2. Gruber AJ, Zavolan M (2019) Alternative cleavage and polyadenylation in health and disease. Nat Rev Genet 20(10):599–614
3. Hoque M et al (2013) Analysis of alternative cleavage and polyadenylation by 3′ region extraction and deep sequencing. Nat Methods 10(2):133–139
4. Berkovits BD, Mayr C (2015) Alternative 3′ UTRs act as scaffolds to regulate membrane protein localization. Nature 522(7556):363–367

5. Di G, Nishida K, Manley JL (2011) Mechanisms and consequences of alternative polyadenylation. Mol Cell 43(6):853–866
6. Lutz CS, Moreira A (2011) Alternative mRNA polyadenylation in eukaryotes: an effective regulator of gene expression. Wiley Interdiscip Rev RNA 2(1):22–31
7. Mayr C (2016) Evolution and biological roles of alternative 3′UTRs. Trends Cell Biol 26(3):227–237
8. Tian B, Manley JL (2017) Alternative polyadenylation of mRNA precursors. Nat Rev Mol Cell Biol 18(1):18–30
9. Ji Z et al (2009) Progressive lengthening of 3′ untranslated regions of mRNAs by alternative polyadenylation during mouse embryonic development. Proc Natl Acad Sci USA 106(17):7028–7033
10. Miura P et al (2013) Widespread and extensive lengthening of 3′ UTRs in the mammalian brain. Genome Res 23(5):812–825
11. Beaudoing E et al (2000) Patterns of variant polyadenylation signal usage in human genes. Genome Res 10(7):1001–1010
12. Proudfoot NJ, Brownlee GG (1976) 3′ non-coding region sequences in eukaryotic messenger RNA. Nature 263(5574):211–214
13. Danckwardt S et al (2007) Splicing factors stimulate polyadenylation via USEs at non-canonical 3′ end formation signals. EMBO J 26(11):2658–2669
14. Moreira A et al (1998) The upstream sequence element of the C2 complement poly(A) signal activates mRNA 3′ end formation by two distinct mechanisms. Genes Dev 12(16):2522–2534
15. Natalizio BJ et al (2002) Upstream elements present in the 3′-untranslated region of collagen genes influence the processing efficiency of overlapping polyadenylation signals. J Biol Chem 277(45):42733–42740
16. Nunes NM et al (2010) A functional human Poly(A) site requires only a potent DSE and an A-rich upstream sequence. EMBO J 29(9):1523–1536
17. Li W et al (2015) Systematic profiling of poly(A)+ transcripts modulated by core 3′ end processing and splicing factors reveals regulatory rules of alternative cleavage and polyadenylation. PLoS Genet 11(4):e1005166
18. Shi Y et al (2009) Molecular architecture of the human pre-mRNA 3′ processing complex. Mol Cell 33(3):365–376
19. de Klerk E et al (2012) Poly(A) binding protein nuclear 1 levels affect alternative polyadenylation. Nucleic Acids Res 40(18):9089–9101
20. Kubo T et al (2006) Knock-down of 25 kDa subunit of cleavage factor Im in Hela cells alters alternative polyadenylation within 3′-UTRs. Nucleic Acids Res 34(21):6264–6271
21. Lackford B et al (2014) Fip1 regulates mRNA alternative polyadenylation to promote stem cell self-renewal. EMBO J 33(8):878–889
22. Takagaki Y et al (1996) The polyadenylation factor CstF-64 regulates alternative processing of IgM heavy chain pre-mRNA during B cell differentiation. Cell 87(5):941–952
23. Curinha A et al (2014) Implications of polyadenylation in health and disease. Nucleus 5(6):508–519
24. Pereira-Castro I, Moreira A (2021) On the function and relevance of alternative 3′-UTRs in gene expression regulation. Wiley Interdiscip Rev RNA e1653
25. Sandberg R et al (2008) Proliferating cells express mRNAs with shortened 3′ untranslated regions and fewer microRNA target sites. Science 320(5883):1643–1647
26. Sommerkamp P et al (2020) Differential Alternative Polyadenylation Landscapes Mediate Hematopoietic Stem Cell Activation and Regulate Glutamine Metabolism. Cell Stem Cell 26(5):722-738e7
27. Pai AA et al (2016) Widespread Shortening of 3′ Untranslated Regions and Increased Exon Inclusion Are Evolutionarily Conserved Features of Innate Immune Responses to Infection. PLoS Genet 12(9):e1006338
28. Mayr C, Bartel DP (2009) Widespread shortening of 3′UTRs by alternative cleavage and polyadenylation activates oncogenes in cancer cells. Cell 138(4):673–684
29. Morris AR et al (2012) Alternative cleavage and polyadenylation during colorectal cancer development. Clin Cancer Res 18(19):5256–5266
30. Cheng LC et al (2020) Widespread transcript shortening through alternative polyadenylation in secretory cell differentiation. Nat Commun 11(1):3182
31. Chen M et al. (2008) 3′ UTR lengthening as a novel mechanism in regulating cellular senescence. Genome Res
32. Hilgers V et al (2011) Neural-specific elongation of 3′ UTRs during Drosophila development. Proc Natl Acad Sci U S A 108(38):15864–15869
33. Domingues RG et al (2016) CD5 expression is regulated during human T-cell activation by alternative polyadenylation, PTBP1, and miR-204. Eur J Immunol 46(6):1490–1503
34. Braz SO et al (2017) Expression of Rac1 alternative 3′ UTRs is a cell specific mechanism with a function in dendrite outgrowth in cortical neurons. Biochim Biophys Acta Gene Regul Mech 1860(6):685–694
35. Pinto PA et al (2011) RNA polymerase II kinetics in polo polyadenylation signal selection. EMBO J 30(12):2431–2444
36. de Morree A et al (2019) Alternative polyadenylation of Pax3 controls muscle stem cell fate and muscle function. Science 366(6466):734–738
37. An JJ et al (2008) Distinct role of long 3′ UTR BDNF mRNA in spine morphology and synaptic plasticity in hippocampal neurons. Cell 134(1):175–187
38. Dzhagalov I, Dunkle A, He YW (2008) The anti-apoptotic Bcl-2 family member Mcl-1 promotes T lymphocyte survival at multiple stages. J Immunol 181(1):521–528
39. Kozopas KM et al (1993) MCL1, a gene expressed in programmed myeloid cell differentiation, has sequence similarity to BCL2. Proc Natl Acad Sci 90(8):3516–3520
40. Michels J, Johnson PW, Packham G (2005) Mcl-1. Int J Biochem Cell Biol 37(2):267–271
41. Senichkin VV et al (2019) Molecular comprehension of Mcl-1: from gene structure to cancer therapy. Trends Cell Biol 29(7):549–562
42. Opferman JT et al (2003) Development and maintenance of B and T lymphocytes requires antiapoptotic MCL-1. Nature 426(6967):671–676
43. Fernandez-Marrero Y et al (2016) Survival control of malignant lymphocytes by anti-apoptotic MCL-1. Leukemia 30(11):2152–2159
44. Campbell KJ et al (2018) MCL-1 is a prognostic indicator and drug target in breast cancer. Cell Death Dis 9(2):19
45. Song L et al (2005) Mcl-1 regulates survival and sensitivity to diverse apoptotic stimuli in human non-small cell lung cancer cells. Cancer Biol Ther 4(3):267–276
46. Fleischer B et al (2006) Mcl-1 is an anti-apoptotic factor for human hepatocellular carcinoma. Int J Oncol 28(1):25–32
47. Kearse M et al (2012) Geneious Basic: an integrated and extendable desktop software platform for the organization and analysis of sequence data. Bioinformatics 28(12):1647–1649
48. Pfaffl MW (2001) A new mathematical model for relative quantification in real-time RT-PCR. Nucleic Acids Res 29(9):e45
49. Liu H, Naismith JH (2008) An efficient one-step site-directed deletion, insertion, single and multiple-site plasmid mutagenesis protocol. BMC Biotechnol 8:91
50. Hwang HW, Wentzel EA, Mendell JT (2009) Cell-cell contact globally activates microRNA biogenesis. Proc Natl Acad Sci U S A 106(17):7016–7021
51. Sanjana NE, Shalem O, Zhang F (2014) Improved vectors and genome-wide libraries for CRISPR screening. Nat Methods 11(8):783–784
52. Schindelin J et al (2012) Fiji: an open-source platform for biological-image analysis. Nat Methods 9(7):676–682

53. Rueden CT et al (2017) Image J2: ImageJ for the next generation of scientific image data. BMC Bioinformat 18(1):529
54. Berg S et al (2019) ilastik: interactive machine learning for (bio) image analysis. Nat Methods 16(12):1226–1232
55. Vorkel D, Haase R (2020) GPU-accelerating ImageJ Macro image processing workflows using CLIJ. arXiv preprint arXiv:2008.11799
56. Haase R et al (2020) Interactive design of GPU-accelerated Image Data Flow Graphs and cross-platform deployment using multi-lingual code generation. bioRxiv. https://doi.org/10.1101/2020.11.19.386565
57. Haase R et al (2020) CLIJ: GPU-accelerated image processing for everyone. Nat Methods 17(1):5–6
58. Ho TK (1998) The random subspace method for constructing decision forests. IEEE Trans Pattern Anal Mach Intell 20(8):832–844
59. Schmidt U et al (2018) Cell detection with star-convex polygons. In international conference on medical image computing and computer-assisted intervention. Springer
60. Ollion J et al (2013) TANGO: a generic tool for high-throughput 3D image analysis for studying nuclear organization. Bioinformatics 29(14):1840–1841
61. Stringer C et al (2021) Cellpose: a generalist algorithm for cellular segmentation. Nat Methods 18(1):100–106
62. Legland D, Arganda-Carreras I, Andrey P (2016) MorphoLibJ: integrated library and plugins for mathematical morphology with ImageJ. Bioinformatics 32(22):3532–3534
63. Bingle CD et al (2000) Exon skipping in Mcl-1 results in a bcl-2 homology domain 3 only gene product that promotes cell death. J Biol Chem 275(29):22136–22146
64. Bae J et al (2000) MCL-1S, a splicing variant of the antiapoptotic BCL-2 family member MCL-1, encodes a proapoptotic protein possessing only the BH3 domain. J Biol Chem 275(33):25255–25261
65. Corkum CP et al (2015) Immune cell subsets and their gene expression profiles from human PBMC isolated by Vacutainer Cell Preparation Tube (CPT) and standard density gradient. BMC Immunol 16:48
66. Gruber AR et al (2014) Global 3′ UTR shortening has a limited effect on protein abundance in proliferating T cells. Nat Commun 5:5465
67. Perciavalle RM et al (2012) Anti-apoptotic MCL-1 localizes to the mitochondrial matrix and couples mitochondrial fusion to respiration. Nat Cell Biol 14(6):575–583
68. Germain M, Duronio V (2007) The N terminus of the anti-apoptotic BCL-2 homologue MCL-1 regulates its localization and function. J Biol Chem 282(44):32233–32242
69. Jamil S et al (2005) A proteolytic fragment of Mcl-1 exhibits nuclear localization and regulates cell growth by interaction with Cdk1. Biochem J 387(Pt 3):659–667
70. Pawlikowska P et al (2010) ATM-dependent expression of IEX-1 controls nuclear accumulation of Mcl-1 and the DNA damage response. Cell Death Differ 17(11):1739–1750
71. Neve J et al (2016) Subcellular RNA profiling links splicing and nuclear DICER1 to alternative cleavage and polyadenylation. Genome Res 26(1):24–35
72. Labi V, Schoeler K, Melamed D (2019) miR-17 ~ 92 in lymphocyte development and lymphomagenesis. Cancer Lett 446:73–80
73. He L, Hannon GJ (2004) MicroRNAs: small RNAs with a big role in gene regulation. Nat Rev Genet 5(7):522–531
74. Oliveira MS et al (2019) Cell Cycle Kinase Polo Is Controlled by a Widespread 3′ Untranslated Region Regulatory Sequence in Drosophila melanogaster. Mol Cell Biol 39(15):e00581–18
75. Proudfoot NJ (2011) Ending the message: poly(A) signals then and now. Genes Dev 25(17):1770–1782
76. Zhao Y et al (2017) Demethylzeylasteral inhibits cell proliferation and induces apoptosis through suppressing MCL1 in melanoma cells. Cell Death Dis 8(10):e3133
77. Whitaker RH, Placzek WJ (2020) MCL1 binding to the reverse BH3 motif of P18INK4C couples cell survival to cell proliferation. Cell Death Dis 11(2):156
78. Widden H, Placzek WJ (2021) The multiple mechanisms of MCL1 in the regulation of cell fate. Commun Biol 4(1):1029
79. Morciano G et al (2016) Mcl-1 involvement in mitochondrial dynamics is associated with apoptotic cell death. Mol Biol Cell 27(1):20–34
80. Morciano G et al (2016) Intersection of mitochondrial fission and fusion machinery with apoptotic pathways: Role of Mcl-1. Biol Cell 108(10):279–293
81. Rasmussen ML et al (2018) A Non-apoptotic function of MCL-1 in promoting pluripotency and modulating mitochondrial dynamics in stem cells. Stem Cell Reports 10(3):684–692
82. Rasmussen ML et al (2020) MCL-1 inhibition by selective BH3 mimetics disrupts mitochondrial dynamics causing loss of viability and functionality of human cardiomyocytes. IScience 23(4):101015
83. Leonard AP et al (2015) Quantitative analysis of mitochondrial morphology and membrane potential in living cells using high-content imaging, machine learning, and morphological binning. Biochim Biophys Acta 1853(2):348–360
84. Chen H et al (2003) Mitofusins Mfn1 and Mfn2 coordinately regulate mitochondrial fusion and are essential for embryonic development. J Cell Biol 160(2):189–200
85. Cohen MM, Tareste D (2018) Recent insights into the structure and function of Mitofusins in mitochondrial fusion. F10000Res https://doi.org/10.12688/f1000research.16629.1
86. Mayr C (2017) Regulation by 3′-Untranslated Regions. Annu Rev Genet 51:171–194
87. Drake JA et al (2006) Conserved noncoding sequences are selectively constrained and not mutation cold spots. Nat Genet 38(2):223–227
88. Duret L, Dorkeld F, Gautier C (1993) Strong conservation of non-coding sequences during vertebrates evolution: potential involvement in post-transcriptional regulation of gene expression. Nucleic Acids Res 21(10):2315–2322
89. Li YQ et al (2020) FNDC3B 3′-UTR shortening escapes from microRNA-mediated gene repression and promotes nasopharyngeal carcinoma progression. Cancer Sci 111(6):1991–2003
90. Mogilyansky E, Rigoutsos I (2013) The miR-17/92 cluster: a comprehensive update on its genomics, genetics, functions and increasingly important and numerous roles in health and disease. Cell Death Differ 20(12):1603–1614
91. Thomas LW et al (2012) Serine 162, an essential residue for the mitochondrial localization, stability and anti-apoptotic function of Mcl-1. PLoS ONE 7(9):e45088
92. Chong SJF et al (2020) Noncanonical cell fate regulation by Bcl-2 proteins. Trends Cell Biol 30(7):537–555
93. Yu R et al (2019) Human Fis1 regulates mitochondrial dynamics through inhibition of the fusion machinery. EMBO J 38:e99748
94. Tilokani L et al (2018) Mitochondrial dynamics: overview of molecular mechanisms. Essays Biochem 62(3):341–360
95. Joaquim M, Escobar-Henriques M (2020) Role of mitofusins and mitophagy in life or death decisions. Front Cell Dev Biol 8:572182
96. Milani M et al (2019) DRP-1 functions independently of mitochondrial structural perturbations to facilitate BH3 mimetic-mediated apoptosis. Cell Death Discov 5:117